Bone ingrowth and medial tibial collapse analysis using finite element method in cementless tibial component of primary total knee arthroplasty.

MSc Thesis

Mauricio C. Saldivar

Technische Universiteit Delft

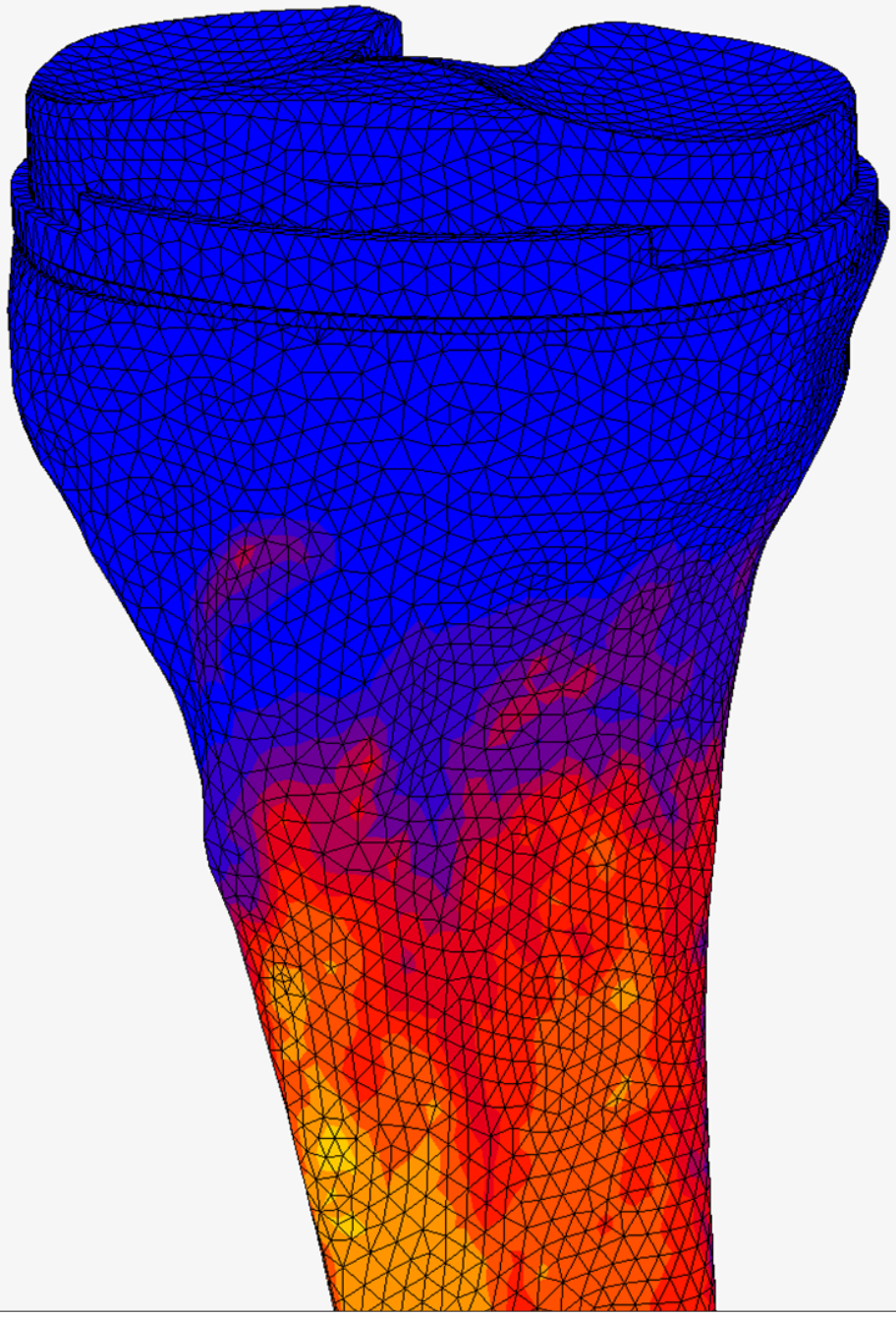

TU Delft Delft University of Technology

Challenge the future

Bone ingrowth and medial tibial collapse analysis using finite element method in cementless tibial component of primary total knee arthroplasty.

MSc Thesis

by

Mauricio C. Saldivar

in partial fulfillment of the requirements for the degree of

Master of Science
Biomedical Engineering, biomaterials and tissue biomechanics track

at the Delft University of Technology,

to be defended publicly on Monday August 27, 2018 at 11:15 AM.

Student number: 4618114
Supervisors: Dr. Ir. D. Janssen,
Prof. Dr. Ir. N. Verdonschot,
Prof. Dr. Ir. A. Zadpoor.

TU Delft Delft University of Technology

Contents

Abstract

Our ageing, numerous, and increasingly overweight population demands better implant designs and testing methods, reducing the amount of total revision surgeries. To achieve this, more realistic finite element method (FEM) assessment models are a great approach to reduce time and costs of the implant design process. FEM models could be used to evaluate implant performance against several of the main causes of revision, such as lack of bone ingrowth and medial tibial collapse. Failed bone ingrowth of the tibial component can result in early loosening, suggested to occur due to high micromotions at the implant interface. Additionally, post operative misalignment, high patient BMI, and stumbling accidents can cause medial tibial collapse. These phenomena have been assessed via FEM, for which having realistic simulations is important to obtain reliable results. For a realistic simulation, adequate constitutive model, activity loads, and boundary conditions need to be selected. Also, the implantation process must be included to account for intra-surgical bone deformations and softening. The purpose of this study was to investigate which constitutive model better predicts bone deformations during implantation and their effect on subsequent micromotions, bone ingrowth, and medial collapse. Extent of ingrowth results were compared to retrieval data, and the collapse results to risk threshold values.

A FEM model was created from a CT-scanned tibia implanted with a Monoblock and a Persona (Zimmer, Inc., Warsaw, IN) trabecular metal tibial components. Four activities were considered: gait, sitting, stair walking, and cycling. Additionally, four different heterogeneous isotropic material models were used: A linear elastic (LE), a softening Von Mises (sVM) model, an ideal isotropic crushable foam (iICF) model, and a hardening isotropic crushable foam Model (hICF) model. The volumetric plastic strain based hardening function of the latter model was mathematically demonstrated and validated against existing data. For the three plastic models, implantation was performed prior to the micromotion and medial collapse analysis. The resulting micromotions were compared to an ingrowth threshold of $40\mu m$ to estimate extent of ingrowth. The same material models were used to evaluate medial collapse under stumbling conditions. The ingrowth results of the Monoblock were compared to retrieval data on ingrowth to assess equivalences between the simulations and reality. The results of the Persona implant were compared to those of the NexGen to observe differences in implant performance.

The hardening function was able to predict yield surface growth when compared to experimental data. For the implantation simulations, the sVM model presented the most volume of plastic elements around the implant when compared to both the iICF and the hICF models. Different patterns of ingrowth were observed when comparing the simulation results with the retrieval data. The hICF and the sVM models were the best to predict ingrowth when compared to the retrieval data, where the latter under-predicted ingrowth and the former over-predicted it. The LE model results were incapable of predicting ingrowth, especially in the regions where press-fit conditions should be present. For medial tibial collapse, the sVM model results presented structural instabilities at relatively low loading thresholds. The iICF model results were incapable to predict medial collapse due to material instabilities. The hICF model was able to predict collapse without sudden structural and material instabilities.

Implantation results demonstrate the importance of using ICF plastic models in cementless implant analysis, as it provides the necessary contact stresses and adequate concentration of plasticised bone around the implant interface. Although overall tray ingrowth results remained inside the standard deviation of the retrieval data, differences in the ingrowth pattern suggest it is better to use loads obtained from musculoskeletal models rather than patient recordings. Bone ingrowth results of every material model were not fully equivalent to the retrieval data, suggesting extra modelling considerations are required. Using a sVM or a hICF model is suggested for further micromotions and ingrowth research. Ingrowth results show that the added complexity between the LE and the plastic models was enough to predict that the Persona implant was not going to outperform the NexGen, but not enough to predict its failure. Differences in collapse behaviour between material models showed important material and structural instabilities that must be considered in future medial collapse studies. Although progress was achieved, further research is required to realistically simulate the studied phenomena.

1. Introduction

1.1. Total knee arthroplasty: Revision and mechanisms of failure

Functional impairment of the knee leads to a procedure known as primary total knee arthroplasty (TKA) [1]. Among its many variations, TKA has a success rate of 97% five and ten years after the surgery [2]. However, between 2009 and 2013, 337,597 TKA revisions occurred in the U.S.A. [3]. That sums to a cost of $2.7 billion (USD), which is expected to increase to $13 billion (USD) by 2030. Further, revision survival rate drops to 60% after the second surgery [4]. This means a higher risk of continuous surgeries after failure of primary arthroplasty, which increases patient morbidity and burden. These are reasons to optimise implant performance and decrease revision rates.

According to Sharkey et al. [5], loosening (39.9%) was the main reason for TKA revision, followed by infection (27.4%), instability (7.5%), and periprosthetic fracture (4.7%). In this study of 2014, polyethylene (PE) wear was only present in 3.5% of revisions, compared with 25% in 2002 [6]. Wear decreased by high cross linking and vitamin E doping the PE matrix. Although infection is still a relevant problem, it is caused by biological factors. Therefore, PE wear and infection are not included in the present study.

The remaining main failure mechanisms are loosening and instability, which are closely interlinked. Loosening is defined as "*extensive localised bone debonding or resorption, resulting in failed fixation without infection*" (Harris et al., 1976) [7]. Additionally, instability was defined as "*every failure caused by component loosening, bone loss, wear, prosthetic breakage, component sizing, fracture, and collateral ligament failure*" (Vince et al., 2006) [8]. Thus, loosening means that the implant will fail to remain fixated, while instability means high and non-functional movement of the implant relative to the bone. Therefore, it can be assumed that both phenomena can be studied together, as the latter can be considered a consequence of the former.

Most biomechanical studies focus on evaluating one specific type of implant. An implant can be classified by its fixation method as cemented, cementless, and hybrid cemented [9]. While cemented implants achieve fixation by inserting a layer of cement around the interface, cementless implants achieve fixation by press-fitting the implant into the bone [9]. A cementless implant success depends on the ingrowth capability of bone into the surface of the implant [10]. Patients who get these implants are generally younger, more active, and with better bone quality than patients with cemented implants [11].

1.2. Biomechanical failure mechanisms in cementless TKA

The success rate of cemented and cementless implants after ten years is 95.3% and 95.6% respectively [12], but their failure mechanisms are different. For cementless implants, there are three main biomechanical mechanisms of failure that involve instability and loosening. 1) Early instability caused by lack of bone ingrowth; 2) Failure by medial tibial collapse and excessive migration; 3) Long term loosening and instability due to remodelling. These mechanisms are introduced below.

1.2.1. Early instability and lack of bone ingrowth

Radiolucent lines between the implant and the bone were first observed in X-rays by Charnley et al. [13], mostly appearing in the tibial component (Figure 1.1). In 1977, Lotke et al. [14] discovered that these lines were areas in which fibrocartilaginous connective tissue has grown in the bone-implant interface. When radiolucent lines were not present, complete healing and successful ingrowth of the bone with the implant occurred. In 1974, Willert et al. [15] found that fibrocartilaginous tissue is induced by relative movements between the implant and the component in the order of microns. These micromotions were formally defined as "*small movements between a prosthesis and the surrounding bone, that are not detectable with conventional radiographic methods*". (Goodman, 1994) [16]. Therefore, it is necessary to reduce peri-prosthetic micromotions through an adequate

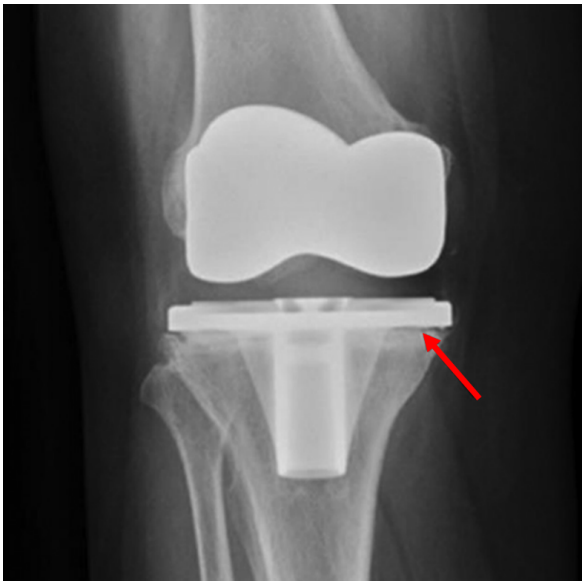

Figure 1.1: The red arrow points towards radiolucent lines in the bone-implant interface present in TKA x-ray scan, which are commonly associated with lack of ingrowth and presence of fibrocartilaginous tissue (figure obtained from [21]).

implant design to secure ingrowth and prevent early instability.

Micromotions are related to bone ingrowth by a threshold value. In 1992, Engh et al. [17] reported motions up to 40 μm in areas where bone ingrowth occurred, and 150μm of micromotions in areas were fibrous tissue was present. Jasty et al. [18] found the same threshold for ingrowth after an in vivo micromotions study. Another study shows that just a few cycles of micromotions per day are enough to interrupt bone ingrowth [19]. Also, the process of fibrocartilaginous growth into the interface can be reversed if the micromotions are interrupted [16]. The low Young's modulus of fibrous tissue and the simple lack of ingrowth in the interface explains early implant loosening and motion [20].

1.2.2. Medial tibial collapse

The second biomechanical reason of failure involves mechanical overload. It is described as failure due to loosening on the medial side of the tibial component, followed by medial sinking and lateral liftoff due to high compression and torsion [22] (Figure 1.2). There are two main factors correlated to medial tibial collapse. The first is post operative varus alignment, which was correlated with medial tibial collapse in early retrieval studies [23, 24]. This misalignment may come from post-surgical errors or excessive early migration, and explains how strains significantly increase when post-operative varus angle is higher than 5° [25]. Besides misalignment, medial collapse is also correlated with a high body mass index (BMI) [26–28]. Also, higher migration and loosening rates were found in patients with higher body mass index (BMI) [29], suggesting that fatigue and sinking of the medial bone can occur after a specific stresses limit.

It can be assumed that medial collapse is mainly influenced by a combination of higher stresses due to increased varus alignment. This can be further increased if the patient has a high BMI. Surprisingly, no correlation between age and collapse risk was found. Therefore, it can be assumed that high BMI leads to higher loads and stresses, leading to higher post operative varus alignment, which in turn increases medial stresses. This positive feedback loop leads to medial collapse at 8° of varus alignment, threshold defined by Berend et al. [26].

1.2.3. Long term instability and loosening due to bone remodelling

Remodelling was first explained by Julius Wolff and his bone adaptation law of 1870 [31]. The law helps to explain how the implant geometry and stiffer material properties provoke new loading conditions upon the bone after primary surgery [32]. This results in remodelling and bone resorption around the implant [7], commonly referred to as stress shielding. Several theories have been developed to

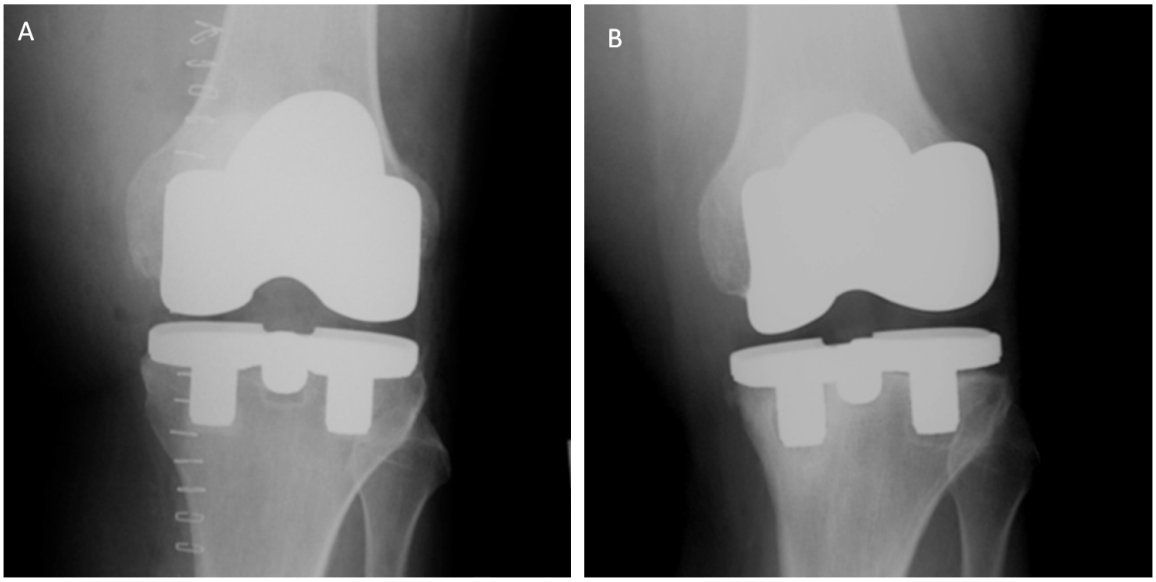

Figure 1.2: A) Immediate post-operative neutral alignment. B) Medial collapse caused by excessive varus tilt. The Figure was obtained from [30].

numerically describe stress shielding. These theories have taken different variables to describe the remodelling phenomenon: A poroelastic strain theory by Cowin and Hegedus [33, 34]; a stress based theory by Beaupre, Orr and Carter [35]; an orientation and density based theory by Jacobs [36]; a damage anisotropic repair model by Doblare and Garcia [37]; and a strain energy density (SED) based isotropic remodelling theory by Huiskes et al. [38].

For the previous listed theories, the SED theory of Huiskes et al. [38] appears to be one of the most studied. It proposes a numerical representation of remodelling, where the rate of bone density change depends on the SED at implanted conditions. A reference SED value (SED of the intact bone), and a ”threshold” dead zone value (a proportion of the reference SED) are required to define the bone density change function. When the SED is below the dead zone, bone resorption occurs, when it is inside the dead zone, the density rate will be zero (known as lazy zone), and beyond the dead zone the rate increases (bone deposition).

1.3. FEM in instability and loosening analysis

Finite element method (FEM) has been used to study the previously described failure mechanisms since the early days of total joint arthroplasty. FEM helps to computationally assess the state of bone tissue and its response to implant stimuli [39]. In an early review of FEM state of the art in orthopaedics, Huiskes et al. [40] concluded that simulations must become more realistic to satisfy the market requirements. A realistic simulation should be able to reduce implant design times and limit the number of revisions, requirements which are still relevant today. As the problems involving TKA failure increase, a more realistic FEM model allows further fine tuning and comparison between different implant designs.

To be able to develop such a realistic FEM model for a cementless implant, it is necessary to understand the evolution and state of the art of TKA implants as well as its biomechanical analysis. FEM models can be classified by the failure mechanism they study. These studies are introduced below and in the following order: 1) Lack of bone ingrowth and micromotions; 2) Medial tibial collapse due to misalignment and overloading; 3) Bone resorption and loosening.

1.3.1. Micromotions and bone ingrowth analysis

Micromotions algorithm

Van der Ploeg et al. [41] demonstrated that using a node-to-face algorithm leads to a better correlation with experimental data. The algorithm considers the implant and bone as separate meshes in contact via linear Coulomb friction. This study introduced the concept of incremental and resulting micromotions. The method consists of four steps. First, an implant contact node is projected into the closest bone element face. Then, the initial position of the node before applying any load is stored. Subsequently, displacements with respect to the bone face for every load increment are tracked (known as incremental micromotions). Finally, after the activity cycle finished, the resulting micromotion of that node is defined as the longest distance between all incremental micromotions.

Forces and loading cycles

In a computational study on micromotions, Chong et al. [42] concluded that full activity loading cycles affect micromotion results the most. Thus, using the full loading cycles is required to have an adequate estimation of bone ingrowth. Beramahni et al. [43] also performed micromotion studies to evaluate the effects of full cycles versus using peak forces only. When using full activity loading cycles, large micromotions occurred at both low and peak forces. This study suggests that micromotions depend on the total force direction changes as much as the magnitude of the force, recommending to use full loading cycles to have more realistic results.

Additionally, the use of patello-femoral tendon forces drastically decreased the amount of micromotions [43]. To include patello-femoral tendon forces it is necessary to have a fully validated musculoskeletal model of every ligament. When a musculoskeletal model is not available, the use of forces obtained from patient recordings via reverse kinematics can be used. These loads can be found in Bergmann et al. [44], which includes recordings from several activities, patients, and implant types. Van der Ploeg et al. [41] also observed that changing the boundary conditions does not influence the micromotion results. Therefore, it is possible to use a small section of the proximal tibia for analysis to save computation time and memory.

Material models

Most of the FEM studies conducted to assess micromotions use linear elastic (LE) models. Studying a cementless implant requires an interference fit in millimetre scale. It is physically impossible for a surgeon to insert an implant with a hammer and achieve a fit in the order of micrometres. A micro-metric interference fit may be estimated by resembling the yield limit of the bone when using a homogeneous model [45]. This interference fit is not valid for a heterogeneous model because the yield is not the same for every bone element. This makes the use of a LE model unrealistic. When trying to accurately predict whether a patient is prone to get a revision surgery due to mechanical failure, a more realistic material model that includes effects of high strains is necessary.

Two isotropic heterogeneous elastic material models characterised for the human tibia are depicted in Keyak et al. [46] and Morgan et al. [47]. Both material models use ash density in an exponential regression system as a mean to obtain the Young's Modulus of every element ($E = a\rho_{ash}^{b}$). The models distinguish between trabecular and cortical bone by a threshold value that defines constants a and b. Also, similar studies provide equations to obtain heterogeneous yield stress values. These can be used to create a simple ideal plastic model [48, 49]. In these cases, yield stress is also obtained from power regression equations that depend on the element's ash density and bone type ($S = c\rho_{ash}^{d}$).

A more complex elastoplastic model validated for the tibia that depends entirely on ash density is found in Keyak et al. [50]. Bone mechanical behaviour starts with a linear elastic section with a Young Modulus ($E = a\rho_{ash}^{b}$). The linear elastic section continues until the yield stress ($S = c\rho_{ash}^{d}$) is reached under a Von Mises criterion. Then, an ideally plastic region follows until a specific strain ϵ_{AB} occurs. Next, a softening region with a negative slope (E_p) is considered until a minimal stress value (σ_{min}) is reached. Finally, a second ideally plastic region is considered, which represents bone failure.

The latter material model was characterised for the femur in Keyak et al. [51]. This was used by Berahmani et al. [52] in an ex vivo femoral micromotions experiment on fresh bone samples. More

specifically, a post-mortem implantation of TKA femoral components was performed. This was followed by a micromotions assessment in several regions of interest (ROI) and comparing them to micromotion FEM analyses. Both the Keyak et al. LE model [46] as well as the softening Von Mises (sVM) model [51] were used in Berahmani et al.'s FEM analyses. They found that the plastic sVM model predicts micromotions better than the LE model, as its results correlated better with the experimental data. However, the use of a sVM criterion was not realistic enough to fully predict experimental micromotions. The study also concluded that it is necessary to simulate implant insertion prior to micromotion analysis. This allows to compensate for the early excessive deformations that reduce the strength limit of the tissue and affect micromotions.

It can be argued that the use of a Von Mises criterion is not realistic enough because bone is pressure dependent. Kelly et al. [53] demonstrated that an isotropic crushable foam (ICF) constitutive model predicts post-yield bone behaviour more accurately than a Von Mises criterion, as it can also reach yield under confined compression conditions. This is a situation that occurs in the tibial implant interface, as the porous trabecular bone is surrounded by the stiffer cortical bone. The ICF model was later validated for a bovine vertebra during an indentation test [54]. This post-yield behaviour could be used for human research, as the properties of bovine trabecular bone are similar to those of a human [55].

There are two considerations that can be taken from the post-yield behaviour of the ICF model. The first is to consider an ideal hardening behaviour. That is, the yield surface will not grow under plastic conditions. This approach can be considered when there is no data on the hardening behaviour of the chosen material. The second and most realistic consideration is to use a hardening/softening function obtained from experimental data on the material. Since there is no information regarding bone hardening for ICF tibial models, a hardening function was obtained based on the permanent volumetric changes of bone. Such function was mathematically demonstrated in this study and validated using bovine trabecular bone hardening plots available in Kelly et al. [54].

Micromotion analyses in tibial components

The previously introduced experiments regarding the use of full loading cycles and complex material models have only been performed in femoral components, but not in tibial components. Most of the tibial component micromotion experiments are outdated and do not have enough complexity to be compared to retrieval or experimental data [45, 56, 57]. Only Fitzpatrick et al. [58] and Hanzlik et al. [59] have performed studies on tibial micromotions by using LE models only. Additionally, they have not been able to accurately simulate ingrowth and compare it with retrieval data.

Simulating implantation before micromotion analysis has only been performed in femoral component studies [52]. As discussed above, it is important to consider implantation before micromotion analysis to account for tissue deformation and softening. Bone tissue deformation produces the press-fit contact stresses for the cementless implant to remain in its position. Bone softening can lead to negative consequences, as surgeons may allow patients to walk home right after surgery, meaning they become active when bone has not healed yet. This can result in more micromotions and less bone ingrowth. Elastoplastic material constitutive models are necessary for this type of analysis, which could potentially predict how much interference fit is enough to have an optimal bone-implant bonding [60].

The previously described work has set the standard for micromotion experiments. To summarise, a face-node algorithm should be used and the simulations should include full activity loading cycles. The consequences of hammering the implant into the bone should be considered to account for post-surgical tissue softening and high deformations. Finally, using an adequate bone material model is necessary. This standard has not yet been validated for tibial components, for which either retrieval or experimental studies could be used.

1.3.2. Medial tibial collapse

Roentgen stereophotogrammetry (RSA) [61] is the preferred method to predict an implant's migration rate. Li et al. [62] compared cemented against cementless implant migration using RSA, observing that the latter reached 80% of their final migration within one month after surgery. Other studies have

compared migration rates among cementless implants [63–66], finding that most of them reached their final position six weeks after surgery. They also found that the final position is mostly accompanied by an increase in varus alignment.

The use of elastoplastic models is necessary to assess medial tibial collapse, due to their capability to account for permanent deformations. These deformations could be tracked under potentially dangerous loadings such as stumbling conditions [67]. Although using such material models should be adequate to assess collapse, most FEM studies have only focused on post-operative alignment analysis. These studies have validated the hypothesis of increased risks when a patient has a post-operative varus alignment, potentially leading to collapse.

Perillo et al. [68] performed a FEM analysis on post-surgical alignment. In this study, they investigated if varus or valgus alignment affected stress concentrations in the bone. The results showed that stresses increased up to 22% when varus alignment was higher than 5° compared to a neutral varus position. This experiment was replicated by Liau et al. [69], who included forces coming from the collateral ligaments. They found 45% higher stresses at 7° varus compared to neutral alignment. The same experiment was conducted by Inoccenti et al. [70], where 6° varus led to 38% more stresses on the medial side and 20% less stresses on the lateral side.

The fact that 80% of migration occurs in early stages after surgery may be explained by post-surgical softening, bone ingrowth, and remodelling. The other 20% may occur only due to remodelling and softening of the later stages. An idea to perform a FEM analysis to simulate implantation and migration might be to include the use of an elastoplastic material model and several different activities to track migration. The model could have an initial stage were ingrowth is calculated, and then set the contact conditions to start a remodelling analysis. The results of such a model could then be compared or validated against RSA studies.

The latter experiment would be the ideal case to study medial tibial collapse mixed with remodelling, but there is a problem. Among the existing tibial remodelling studies, none has achieved validation with clinical data [71–73]. These studies have predicted high bone deposition below the implant stem, a situation that does not occur according to clinical studies [74]. Creating a tibia-specific remodelling subroutine requires much more time and experiments than available for a master thesis project. Therefore it was considered out of the scope of the current study. However, developing a remodelling subroutine for the tibia is necessary to make a model that can predict migration analysis. Thus, this study focused on a simpler experiment that can predict collapse under stumbling conditions, which could be used as a basis for future experiments.

In any case, an instability threshold value for collapse could be obtained for a specific implant under stumbling conditions. Such a collapse threshold could be defined in percentage of body-weight (%BW), as it is a patient specific unit, commonly used in loading studies such as Bergmann et al. [44]. The threshold could also be compared to varus alignment, as it gives information about when the knee becomes unstable. These data could then be used to compare implant performance under collapse conditions.

1.3.3. Mixing bone ingrowth and medial tibial collapse

To create a FEM model capable of interlinking ingrowth and medial tibial collapse, three experiments have to be conducted. 1) An implantation experiment in which an adequate plasticity constitutive material model is validated for the tibia; 2) A micromotion analysis after implantation to obtain bone ingrowth surface; 3) An overloading analysis after implantation to obtain collapse thresholds, and compare them to those of the reviewed literature. Also, the bone ingrowth results have to be compared to retrieval experiments, as in Hanzlik et al. [75].

Nevertheless, even if the previous experiments and FEM simulations could take place, there are still two important considerations. 1) The loads applied for the different experiments should be representative of common activities performed by humans, and they should derive from implant design specific musculoskeletal models. 2) Experimentation via FEM should not only involve one experiment with

one bone that represents the average mechanical properties of a population. Instead, a set of bones with different characteristics that average the population of the validation data should be used, as they give a more accurate representation of what happens in reality [76]. This means that simulations should not only include variations in the constitutive model chosen, but also from loads and density qualities. This allows to observe if the added complexity of the material model is enough to validate retrieval data by using statistical testing. For this, a two one-sided t-test (TOST) can be used, commonly known as an equivalence test [77].

1.4. The NexGen and Persona case study

To study whether the tool that predicts bone ingrowth works, it needs to be validated against retrieval data. Such data was obtained from Hanzlik et al. [75]. In this study, information about the extent of ingrowth (the percentage of the implant surface that presented bone ingrowth) is present for two Zimmer's NexGen trabecular metal implants: Monoblock and Modular. The Monoblock design was chosen for analysis in this thesis, as the number of retrieved knees with this design is higher than the number of knees implanted with the Modular design. Besides, these retrieved knees were not obtained from revision cases, but from successful post-mortem cases. That makes them adequate for corroborating the average case of success.

To compare the FEM model of the NexGen with a second implant, a case study was selected. The design of the NexGen Monoblock was compared with Zimmer's Persona trabecular metal tibial component design. The Persona implant was the new iteration from the NexGen series, and was approved in 2012 [78]. The design remained similar to the NexGen, but the latter was voluntarily removed from the market by Zimmer in 2015 due to a high number of revisions [79]. The retrieval report explained that it was recalled due to "*an increase in complaints of loosening and radiolucent lines*". Those conditions suggest that it failed due to excessive micromotions and lack of bone ingrowth. Therefore, a realistic model should be equivalent to the Monoblock's retrieval data, and predict a worse outcome of bone ingrowth and micromotions for the Persona implant.

1.5. Thesis objective, research questions and hypothesis

For the current study, the thesis objective was to create a finite element model that realistically assesses bone ingrowth and medial tibial collapse of tibial components in TKA. With the next set of research questions. 1) Can a volumetric plastic strain based hardening function be mathematically proven and validated for the tibia? 2) How much does implantation and plastic models affect micromotions and bone ingrowth estimation and validation? 3) How much is medial tibial collapse affected by implant design and constitutive model used? 4) Can these tools be used to assess performance between two similar implants?

Several answers are expected to be obtained from these questions. First, a permanent volumetric strain based hardening function should be able to predict a yield surface under bone confined compression. This is because an ICF model bases its yield surface in an ellipse, which allows to form an equation that relates equivalent Von Mises plastic strain with volumetric plastic strain. Such an equation can then be inserted in the equivalent yield stress equations from Keyak et al., and therefore be able estimate compression hardening.

Second, adding complexity to a material model should make the results more equivalent to the retrieval data, with the most complex staying within the standard deviation. Therefore, the linear elastic model should have the worst performance when comparing with retrieval data, followed by the Von Mises criterion model, the ideal ICF model, and finally the hardening ICF should perform closest to the retrieval data. There is also the possibility that the Von Mises criterion model performs the best. This is because the Von Mises model was specifically developed for the tibia, whereas the ICF models were developed for bovine spines.

For implantation and collapse, high strains should be better described by the ICF models. This is because the ICF takes into account the effects of high compression that happen between the tibial component and the bones, a situation that the softening Von Mises model cannot replicate as it depends

entirely on shear. Further, the plasticity levels (large strain deformations) should concentrate in a thin layer as in previous implantation and indentation experiments [52, 54]. To investigate how realistic a material model is, the plasticity layer thickness around the implant needs to be measured.

The third hypothesis involves the individual activity results. In previous tibial component experiments from Hanzlik et al. [59], the expected micromotions and ingrowth varied depending on the load's maximal magnitude and the changes of orientation of the cycles. These force peaks and orientation varied by activity. Therefore, according to loading cycles obtained from patient recordings [44], stair walking should be the worst activity to be performed, followed by gait. If other activities such as cycling and sitting are also studied, cycling results will most probably show the most ingrowth. This is because its maximal force is pretty small, and is not accompanied by high moments.

Regarding collapse risk thresholds, Zimmerman et al. [80] suggested that a slight stumble involves a force between 700% and 900%BW when falling and landing on one leg. In that case, a stumbling condition that leads to a catastrophic structural instability should occur beyond the threshold of 900%BW. Additionally, any material model that is capable of predicting medial tibial collapse should not show material instabilities before the collapse threshold, as the model should be able to simulate the whole collapse process.

Finally, it is expected that the NexGen Monoblock results show better ingrowth performance than the Persona implant. This is because the Persona implant recall report stated that radiolucent lines were presented in too many patients, which means that the Persona had lower overall ingrowth and possibly larger micromotions. Two reasons might explain why this Persona failure occurred. First, the new tray geometry of the Persona might have provoked the lower performance when comparing to the NexGen. Second, changes in the insert surface geometry changed the kinematics of the implant so that the new loads transmitted to the trabecular tibia would cause higher micromotions. Although the study of both cases is necessary, the latter requires implant specific loads obtained from a musculoskeletal model. As this was not available in this project, the current study focused on studying the first possibility.

2. Methods

The selected implant models for FEM analysis are the Zimmer's NexGen Monoblock and Zimmer's Persona trabecular metal tibial components. Every simulation was performed with Marc Mentat 2015 software. Medial tibial collapse and bone ingrowth were analysed separately. Both analyses were preceded by a computational implantation process in the simulations that used elastoplastic models. The implants were analysed in a set of ten different bone density qualities. Four different material models and four different activities were considered. These 320 different simulations were later combined to obtain the total extent of ingrowth of a population. Ingrowth results were compared to data from Hanzlik et al. [75] via an equivalence test (two one-sided t-tests) [77]. For the medial tibial collapse simulations, the same combination of implant designs, density values, and materials was used. However, the loads were different, as stumbling conditions were applied with increasing total magnitude until structural instability was reached. The 60 simulations were later combined to obtain a mean body weight threshold for collapse. For both bone ingrowth and medial tibial collapse simulations, equivalence tests were performed for the Persona with the NexGen as control. This allowed to observe if there were significant differences in performance between both implants. The details for each step of the process are described below.

2.1. Implant geometries and material properties

NexGen Monoblock implant

As its name implies, the NexGen Monoblock tibial component [81] (Figure 2.1 top) consists of only one permanently assembled part made of different materials. Distally, the implant is composed of 80% porous trabecular tantalum. It contains two 20 mm long hexagonal pegs, which provide press-fit and allow bone ingrowth. A composite of porous tantalum and vitamin E doped highly cross-linked ultra high molecular weight PE layer is proximal to the tantalum. The most proximal part is the PE insert, which was machined from the extension of the composite. An implant size C was selected for the current bone geometry [82].

Persona implant

The Persona model is a modular component and shows several geometrical differences when compared to the Monoblock [83] (Figure 2.1 bottom). It is non-symmetric with respect to the medio-lateral plane (Figure 2.1 bottom). The medial side of the implant is larger than the lateral side and occupies more posterior surface than the Monoblock. The most distal part of the component maintains the two hexagonal pegs, with the medial peg leaning more posterior with respect to the lateral [84]. The properties of the pegs and the most distal part of the tray consist of 80% porous tantalum. The porous tantalum is bonded with a layer of titanium. The insert is assembled into the tray via a locking mechanism. As for the Monoblock, a size C was used for the model.

Table 2.1: Linear elastic material properties used for the simulations of the NexGen and Persona implants.

NexGen			**Persona**		
Material	ν	E [GPa]	Material	ν	E [GPa]
Bone	0.3	$a\rho_{ash}^{b}$[46]	Bone	0.3	$a\rho_{ash}^{b}$[46]
Porous Ta	0.31	3.3	Porous Ta	0.31	3.3
Ta-PE	0.35	4.26	Titanium	0.3	110
PE	0.33	1.17	PE	0.33	1.17

2.2. Bone geometry and mesh creation

The primary geometry of the simulated bone was taken from a CT scan of an 81 year-old patient's right knee. The CT scan was obtained with a resolution of 4 $\frac{bits}{mm}$, and a plane offset of 6 $\frac{layers}{mm}$. The bone

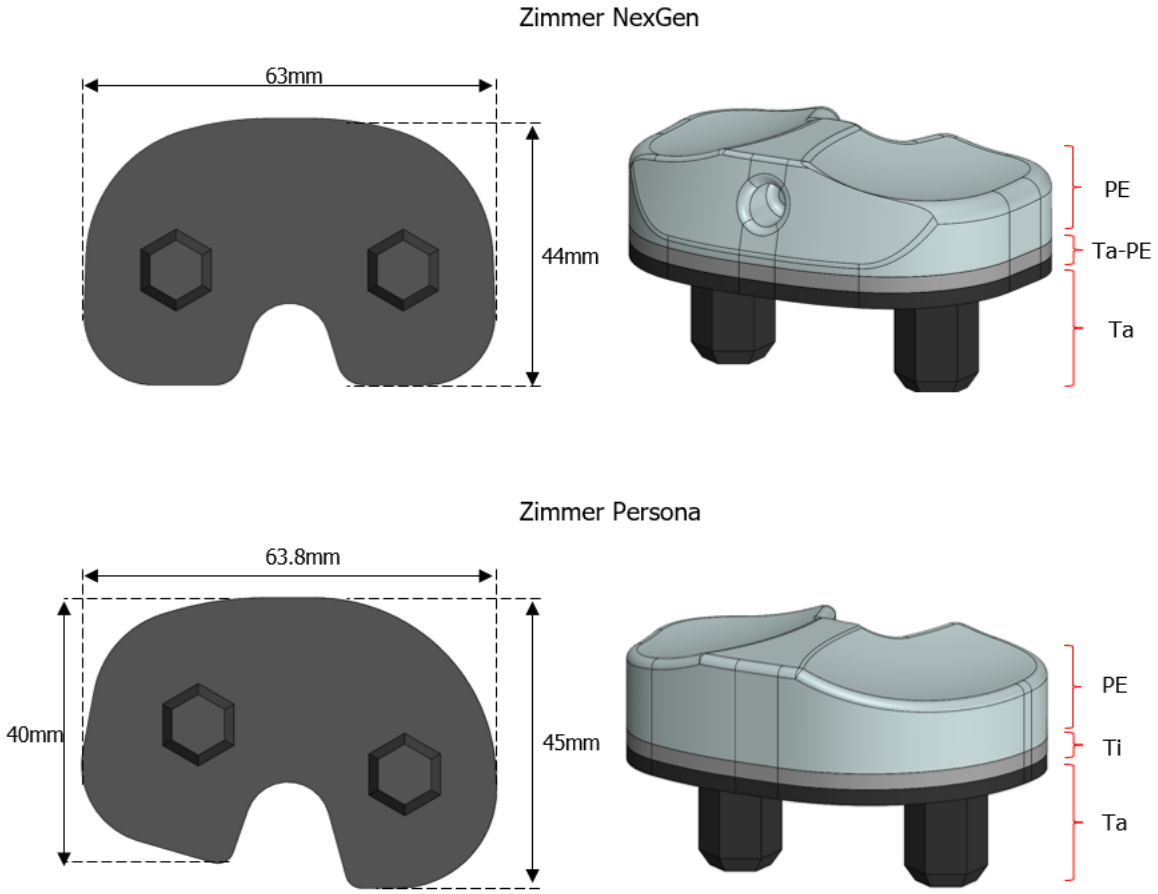

Figure 2.1: Implant geometries and general dimensions for the Zimmer NexGen (top), and Zimmer Persona (bottom) trabecular metal tibial components.

volume was created using Mimics software and different surface meshes with different element sizes of the bone geometry were obtained with Hypermesh using the auto-mesh tool. Both implant geometries were created with Solidworks and the respective surface meshes were created using Hypermesh auto-mesh tool. Ten different meshes were created using four-node tetrahedral elements sized from 0.75 mm to 2.75 mm (Figure 2.2), with steps of 0.20 mm between each mesh.

The surface of the implant meshes were used to virtually resect the tray and peg geometries from the bone via plane intersections. Two different resections were considered: The first one was hexagonal as a perfect fit for the pegs, which was used for LE models (Figure 2.3 A); the second had a cylindrical hole for the hexagonal pegs to be inserted during the simulation, which was used for the plastic material models. The cylindrical hole represents the result of the surgeon's drilling process during the surgical procedures [81, 83] before inserting the implant with a hammer (Figure 2.3 B).

The implants were assembled into the bone using Marc Mentat. Then, a simple simulation was prepared for every perfect fit mesh to evaluate proximal stress convergence. Fixed boundary conditions were assigned into the most distal section of the tibia. A simple load of 1000 Newtons was applied into the PE insert condyles perpendicular to the tibial tray (Figure 2.4 A). The ash bone density values were taken from the original CT scan grey-scale via a Houndsfield unit regression. The Young's modulus values of the bone were obtained from the ash density values using Keyak et al.'s [46] LE model ($E = a\rho_{ash}^{b}$). The chosen Poisson's ratio was $\nu = 0.3$. After the simulations were performed, the average Von Mises

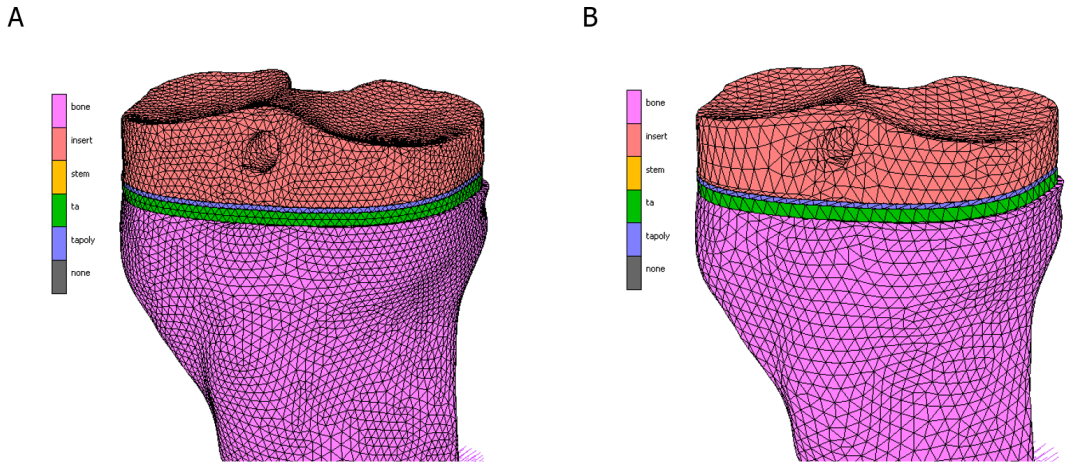

Figure 2.2: Examples of two different NexGen Monoblock tibial component meshes of different size tested for convergence. A) Mesh with element size of 1.65mm. B) Mesh with element size of 2.75mm.

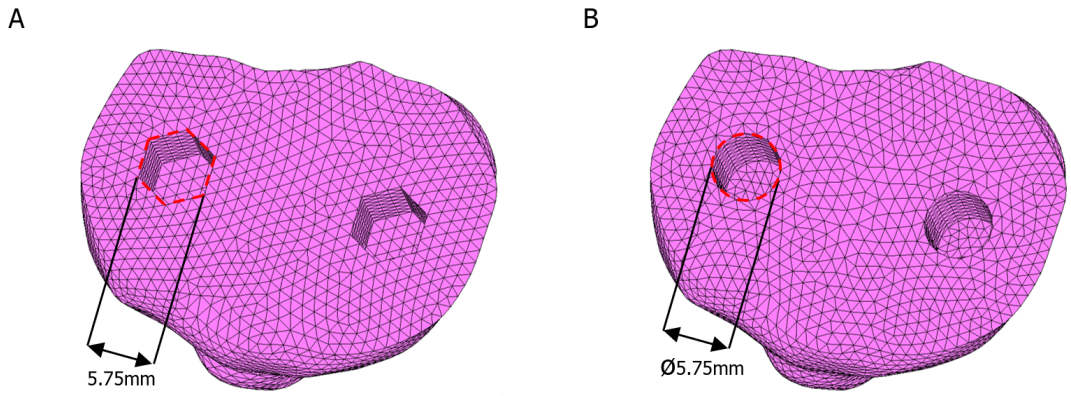

Figure 2.3: Superior view of both bone meshes before implantation. A) Mesh used for elastic material models that had a perfect implant fit. B) Mesh used for elastoplastic models that had a circular hole that represents the drill of the surgeon, which allows the bone to adapt to excessive deformations after implant insertion.

stress of the most proximal part of the bone (2 cm) was plotted against the total number of elements (Figure 2.4 B). The mesh with the least elements that had less than 5% absolute error was selected.

When an element has lower stiffness relative to its neighbours, a material instability can occur [85]. When most stresses occur under compression, instabilities may cause compliant elements to flip inside-out. FEM software usually crash instantly when this situation occurs. To prevent this, the best solution is to have elements large enough so that the compliant elements do not turn inside-out. To further prevent material instabilities, a second mesh test was performed. For this, the same meshes were tested for implantation as this process deforms the bone up to 0.8 mm during the insertion process. Every elastoplastic material model was considered for this test. The mesh that was capable to successfully converge into implantation and passed the stress convergence test was selected. For both implant designs, the final selected element size for the mesh was 2.15 mm.

2.3. Bone density mapping and extrapolation

The bone mineral density (ρ_{ct}) was obtained from the original bone via the micro CT grey-scale Houndsfield values. This function was defined as $\rho_{ct} = p_1 * HU_{value} + p_2$, with $p_1 = 1.5$ and $p_2 = 0.006$,

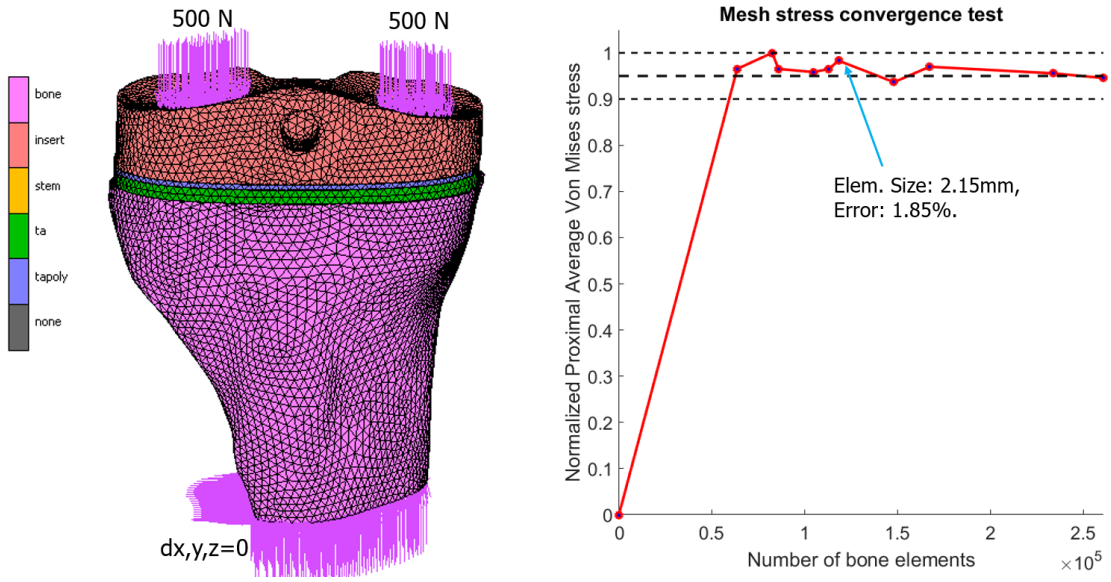

Figure 2.4: Left: Boundary conditions for every mesh convergence test. Right: Mesh stress convergence test results where most mesh sizes passed. The 2.15 mm element size mesh was chosen for analyses.

with ρ_{ct} in Kg/m^3, and HU_{value} in $Hounsfield$. ρ_{ct} was converted to ρ_{ash}, as it is the variable used by all Keyak material models. For that purpose, a linear regression was used with the form $\rho_{ash} = 0.682 * \rho_{ct} + 0.060$, with ρ_{ct} in $\frac{g}{cm^3}$.

A density extrapolation was performed to model a population that represents the statistical data of Hanzlik et al. [75]. This was necessary for two reasons. First, the bone conditions in the analyses should be equivalent to those of the retrieval data [76]. Second, the extrapolation was chosen because only one bone geometry and its density values were available for the current study. As Hanzlik et al. provides information on the age of the retrieved knees, an equation that correlated age with average tibial bone density was used [86]. The equation was obtained from correlations between healthy tibial trabecular bone from deceased humans of different ages, expressed as: $\rho_{ash}[\frac{g}{cm^3}] = -5.5x10^{-5}AGE^2 + 3.8x10^{-3}AGE + 0.28$. To use the equation, it was necessary to obtain equivalent samples from the available bone, just as in Ding et al. [86] experiments. MATLAB was used to isolate four cylinders of trabecular bone from the condyles of the tibia (Figure 2.5).

The cylinder's density was averaged and inserted into the age versus ash density plot (Figure 2.6 step 1). A constant density value $b_o = 0.103\frac{g}{cm^3}$ was added to every bone element to fit Ding's curve (Figure 2.6 step 2). This correction represents a step from osteoporotic bone to a healthy bone, as the equation was obtained from healthy bone samples. Once the original density was adjusted, Ding's equation was used to extrapolate to ten different densities that represent different patients. For the population age (N = 10) the same statistical values as in Hanzlik et al. data were considered (M = 57.7 years, SD = 10.45 years). The ten density values were then divided by the corrected bone value. The resulting multiplier ($A_i = \frac{\rho_{patient,i}}{\rho_{corrected}}$) was used to extrapolate the original healthy bone to every i patient (Figure 2.6 step 3). The result was again corrected to be osteoporotic by subtracting b_o (Figure 2.6 step 4), as the equation is based on healthy bone and the patients who receive an implant should be osteoporotic.

The whole extrapolation process can be expressed as: $\rho_{ash,i} = (\rho_{ash,CT} + b_o)A_i - b_o$. Where $\rho_{ash,i}$ are the density values of each patient i, A_i is the multiplier for every patient, b_o is the osteoporosis correction constant from the original CT scanned bone, and $\rho_{ash,CT}$ is the original ash density of the CT scanned bone. This equation was applied to every element of the CT scanned mesh for every multiplier, which results in the ten patients population. After both the mesh and the ten different sets of densities were defined, the next step was to define the material models.

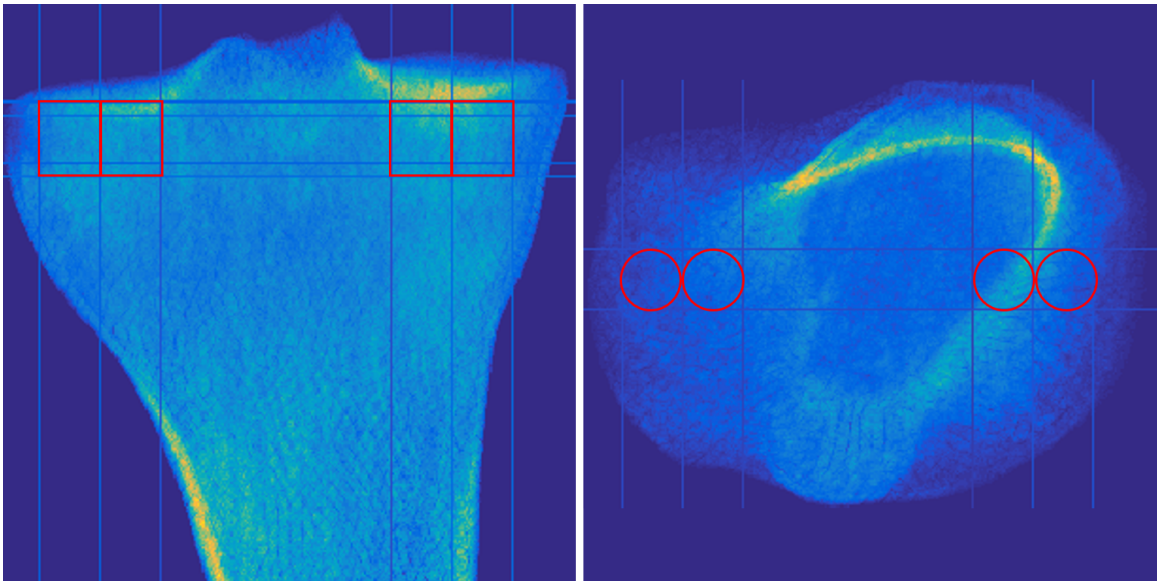

Figure 2.5: Cylinder shaped sections marked in red of the tibia CT scan that were isolated as sample data to extrapolate the whole bone density. Left: anterior view of the DEXA scan. Right: Superior view of the DEXA scan.

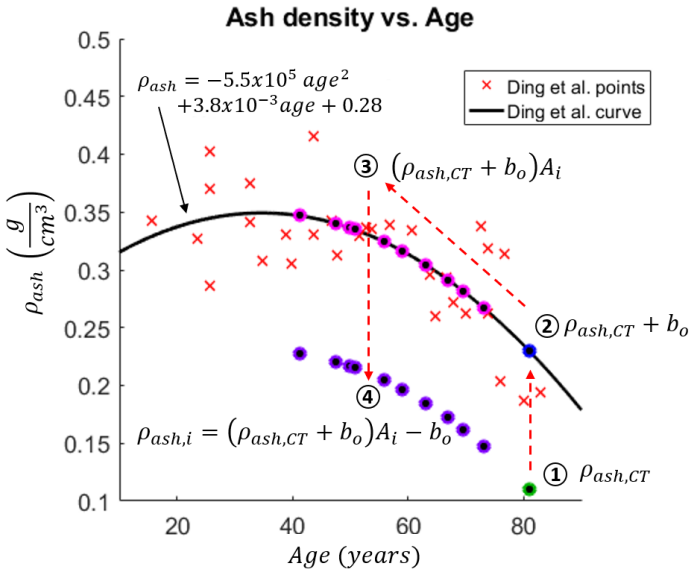

Figure 2.6: Steps performed for extrapolating the original ash density values to the ten osteoporotic sets based on the data of Ding et al. [86]. 1) The CT-scanned average bone density values (green point). 2) CT-scanned ash density corrected to fit Ding et al.'s curve (blue point). 3) Average density points of the chosen population that fits Hanzlik et al.'s data [75] (magenta points). 4) Corrected average density values used in the simulations of the current study (purple points).

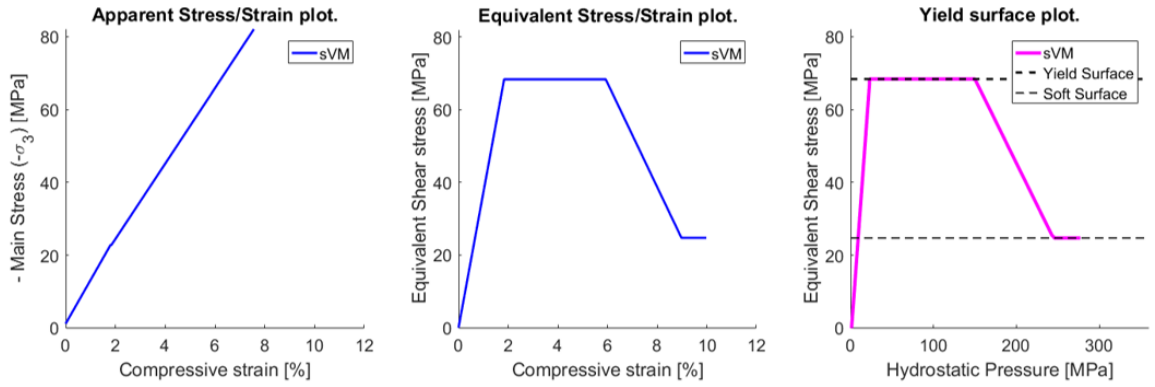

Figure 2.7: Softening Von Mises (sVM) criterion elastoplastic model based on Keyak et al.'s bone model under confined conditions [50]. Left: Apparent stress versus strain plot. Centre: Equivalent Von Mises stress versus strain plot. Right: Equivalent Von Mises versus hydrostatic pressure plot, which shows the model's yield surface behaviour.

2.4. Material models

The four chosen isotropic heterogeneous material models were: The linear elastic (LE) model from Keyak et al. [46], the softening Von Mises (sVM) criterion elastoplastic model from Keyak et al. [50], an ideal crushable foam (iICF) model from Kelly et al. [54], and a hardening version of the previous model (hICF). Ash density values were used to define most of the properties of every material model which are described in detail below.

Linear Elastic (LE) model

In this heterogeneous model, the Young's modulus E is obtained from $E = a\rho_{ash}^{b}$, where a and b depend on the ash density ρ_{ash}. Additionally, a and b constants change its value when the bone element is trabecular, cortical, or in a state of transformation. This material model was also used for the elastic part of the other material models. The chosen Poisson's ratio was $\nu = 0.3$. Formally, it can be written as:

$$E(\rho_{ash}) = \begin{cases} 33900\rho_{ash}^{2.2} & \text{for} \in \rho_{ash} \leq 0.27\frac{g}{cm^3} \\ 10200\rho_{ash}^{2.01} & \text{for} \in \rho_{ash} \geq 0.6\frac{g}{cm^3} \\ 5307\rho_{ash} + 469 & \text{for} \in 0.27\frac{g}{cm^3} < \rho_{ash} < 0.6\frac{g}{cm^3} \end{cases} \tag{2.1}$$

Softening Von Mises (sVM) elastoplastic model

Developed by Keyak et al. [50] (Figure 2.7), the model is an elastoplastic material model where yield is defined by an associative flow rule. The yield criterion (f_{VM}) depends on the second deviatoric stress invariant ($q = \sqrt{\frac{3}{2}(S : S)}$), and takes the form $f_{VM} = q - \sigma_y$, with σ_y as the equivalent yield stress. Similar to the Young's modulus, σ_y is defined by an exponential ash density regression ($\sigma_y = c\rho_{ash}^{d}$). Constants c and d also depend on the bone type, defined as:

$$\sigma_y(\rho_{ash}) = \begin{cases} 137\rho_{ash}^{1.88} & \text{for} \in \rho_{ash} \leq 0.317\frac{g}{cm^3} \\ 114\rho_{ash}^{1.72} & \text{for} \in \rho_{ash} > 0.317\frac{g}{cm^3} \end{cases} \tag{2.2}$$

After the equivalent yield stress is reached, a stage of ideal plasticity begins with the expression $\epsilon_{AB} = 0.0728\rho_{ash} - 3.15x10^{-3}$. A softening section follows with plastic softening module $E_p = -4000\rho_{ash}^{2.05}$. The softening continues until a failure stress is reached, which takes the form $\sigma_{min} = 65.1\rho_{ash}^{1.93}$. Failure stress follows by an ideal plastic state.

Ideal Isotropic Crushable Foam (iICF) elastoplastic model

For this model, the post-yield behaviour of the ICF model defined for bovine trabeculae in Kelly et al. [54] was adapted for the knee (Figure 2.8). The ICF model was chosen because Kelly et al. demonstrated to reflect the most realistic behaviour when comparing FEM results of different material models to experimental data (among Von Mises and Mohr Coulomb bone models). The model was

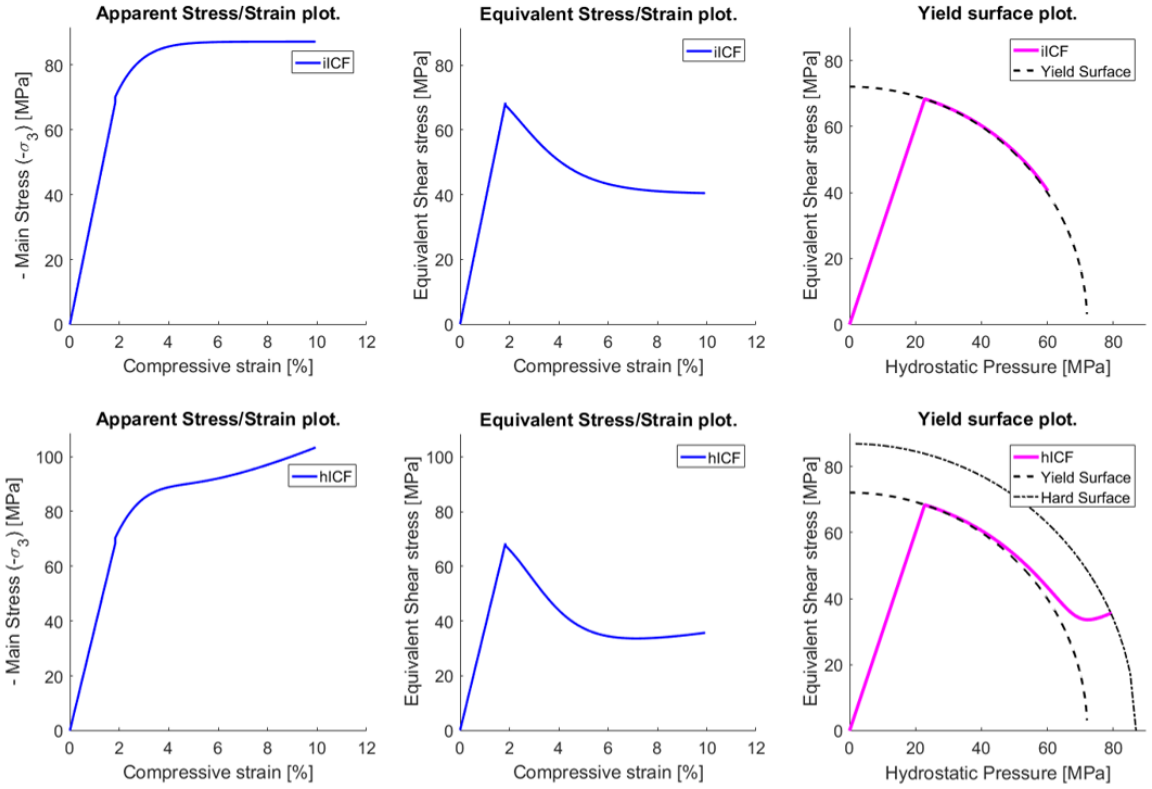

Figure 2.8: Above: Graphical representation of the ideal isotropic crushable foam (ICF) model based on Kelly et al. [54] constants for bovine trabecular bone. Below: Hardening ICF model with the same constants and hardening function demonstrated in this work.

originally created for metallic foams by Deshpande and Fleck [87]. It adds a pressure dependence (first stress tensor invariant $p = -\frac{1}{3}tr(\sigma)$), and a non-associative flow rule (flow vector and yield gradient are not parallel) to the Von Mises yield criterion. The yield function f_{ICF} forms an ellipse with the expression:

$$f_{ICF} = \sqrt{q^2 + \alpha^2 p^2} - q_y \tag{2.3}$$

$$\alpha = \frac{3K}{\sqrt{9 - K^2}} \qquad K = \frac{\sigma_{yo}}{p_{yo}} \qquad q_y = \sigma_y \sqrt{1 + (\frac{\alpha}{3})^2} \tag{2.4}$$

Here, α is the shape of the ellipse, K is the compression yield stress ratio, σ_{yo} the initial yield strength in uniaxial compression, p_{yo} the initial yield stress in hydrostatic compression, q_y the yield stress in pure shear, and σ_y the uniaxial yield strength. For the non-associative part, it follows a flow potential function g_{ICF} with the form:

$$g_{ICF} = \sqrt{q^2 + \beta^2 p^2} \qquad \beta = \frac{3}{\sqrt{2}} \sqrt{\frac{1 - 2\nu_p}{1 + \nu_p}} \tag{2.5}$$

Here, β is the shape of the ellipse of the potential function, and ν_p is the plastic Poisson's ratio. This model can be reduced to the Von Mises criterion model when the shape constants α and β are equal to zero. The initial uniaxial yield strength was obtained using the yield strength equations from Keyak et al. [50] (equation 2.2). According to Kelly et al. [53], the constants to model bovine trabecular bone are $K = 0.95$ and $\nu_p = 0.29$. These constants were selected for the current model for two reasons. First, an equivalent study for the human tibia was not found. Second, the time available for this project to perform the experiments and obtain a characterised ICF model for the knee was not sufficient.

This model was considered ideal (without hardening) due to the lack of information about its behaviour for the tibia. Ideal behaviour is achieved by maintaining the yield strength constant throughout the

simulation ($\sigma_y = \sigma_{yo}$). Although this is valid from the mathematical and computational perspective, not considering hardening (or softening) is too simplistic. Kelly et al. experiments show that the bovine trabecular bone hardens in confined tests. Normally, several experiments are required to obtain a hardening function (h) in terms of equivalent plastic strain (ϵ^p). However, this was not possible within the time frame of the present study. Therefore, hardening simulations were approached via a mathematical model. This was considered as the fourth material model and is described below.

Hardening Isotropic Crushable Foam (hICF) elastoplastic model

To compensate for the lack of experimental data on hardening, a mathematical expression that describes the phenomenon was required. This expression had to replicate Kelly et al.'s data and to be demonstrated mathematically. For this, an equation was developed that is based on volumetric plastic strain (ϵ^p_{vol}) changes, which permanently change the ash density of every element. Changes of ϵ^p_{vol} lead to changes in the uniaxial yield strength equations. Further, when using an ICF model it is possible to correlate the equivalent plastic strain ϵ_p with volumetric plastic strain ϵ^p_{vol} as:

$$\epsilon_{vol} = \frac{\alpha^2}{R}\epsilon_p \tag{2.6}$$

This allows to define uniaxial yield strength (σ_y) and the hardening slope ($\frac{\partial \sigma_y}{\partial \epsilon^p}$) in terms of equivalent plastic strain as:

$$\sigma_y = \frac{\sigma_{yo}}{(1 - \epsilon^p \frac{\alpha^2}{R^2})^d} \tag{2.7}$$

$$\frac{\partial \sigma_y}{\partial \epsilon^p} = \frac{\alpha^2 d \sigma_{yo}}{(R - \alpha^2 \epsilon^p)^{d+1}} \tag{2.8}$$

Here, c and d are defined as in 2.2. The full demonstration of the process to obtain the hardening function is presented in the appendix B. To validate the equation, the computational experiment from Kelly et al. in an 8 mm cube of trabecular bone [54] was replicated. The cube was considered heterogeneous with ash density values $0.01 < \rho_{ash} < 0.73[\frac{g}{cm^3}]$, meaning that the final uniaxial yield strength was $\sigma_{yo} = 66[Mpa]$ as in Kelly et al.'s experiments. The cube was strained to 5% compression in both uniaxial and confined conditions, similar to Kelly et al.'s experiment. The stresses were then plotted together to observe if the hardening equation could replicate Kelly et al.'s experimental data. The same experiment was performed for the other material models to use them as comparison for the hardening results. It was also necessary to develop a compatible subroutine for both ICF models because they are not incorporated in Marc Mentat 2015's software. The subroutine creation process is presented in appendix C.

2.5. Loading definition

Four common activities were selected to evaluate micromotions to answer which activities cause the major impact for bone ingrowth. These activities were walking, stair climbing, cycling, and chair sitting and standing up. The loads were obtained from the Bergmann et al. [44] database. As each loading dataset had too many points, MATLAB was used to extract the representative points for every loading cycle. Exact data points used for each activity are available in appendix A.

To select the loading conditions for medial tibial collapse, a musculoskeletal model that can predict stumbling or a patient recorded stumbling case would be ideal. As this was unavailable, the medial tibial collapse loading conditions were also taken from the Bergmann et al. data. The assumption was that a stumbling patient would land with only one leg stepping towards the front. Therefore, the equivalent "one leg stance" peak load was used. Further, this loading case seems adequate because it has a high normal force and high medial moments (table 2.2), potentially overloading the medial side of the tibia.

For both simulations, the loads were applied in an additional node located in the centre and most distal part of the insert. This was chosen because it is the point in which Bergman et al. defined their loading data. The additional node is connected by rigid links to the upper nodes of each side of the

insert's condyles. This allows transfer of the applied loads into the implant (Figure 2.9 left). The chosen body weight (BW) for every simulation was $96.81kg$, as it is the mean value from the retrieved knees found in Hanzlik et al.'s data. For implantation, displacement boundary conditions were also applied in the node to achieve implant insertion.

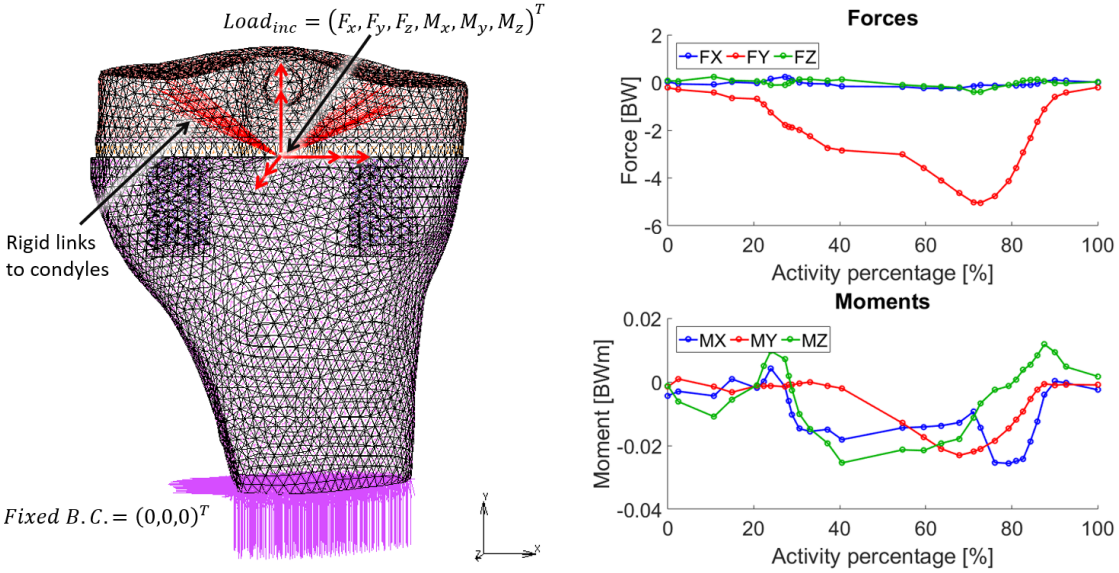

Figure 2.9: Left: Boundary conditions applied in every linear elastic experiment. The loads were referred to an additional node in the implant which is connected to the PE condyles via rigid links. For the plastic experiments, the implant was also separated 20 mm to prepare for implantation. Right: Example of gait loading data applied into the additional node (data for every activity is presented in appendix A).

Table 2.2: Initial loading applied for stumbling conditions in body weight times (BW).

Axis	Lateral/Medial (X)	Superior/Inferior (Y)	Anterior/Posterior (Z)
Force [BW]	0.121	-3.257	-0.123
Moment [BWmm]	-23.948	-3.22	-60.485

2.6. Subroutine processing

The next step was to pre-process the combination of 400 micromotion experiments and 60 medial tibial collapse experiments into the Marc Mentat 2015 software. It was necessary to define the processing of each experiment, including the implantation prelude, and the micromotions and medial tibial collapse subroutines. All pre-processing steps that combine each variable were performed in MATLAB, eliminating possible human errors if done manually. In the next sections, implantation, micromotions, and medial collapse processing algorithms are defined.

Implantation algorithm

All the simulations including a plastic analysis went through an implantation process. To simulate implant insertion in a realistic way is computationally challenging. Controlling insertion via displacement boundary conditions may cause too much buckling, leading to a non-converging process. To be able to insert the implant and adapt the bone to its shape, an interference fit gradient was applied.

An interference fit gradient means that the implant was first negatively fit (shrunk) one centimetre during insertion. This fit was linearly released until implantation was complete. To secure Newton-Raphson convergence, insertion was applied in a set of a hundred increments (Figure 2.10). Therefore, by the end of insertion, the negative interference disappeared and most of the buckling was prevented. Although this definitely does not happen in real life, the pegs still force a fit with the drill hole. This process is more realistic than just assuming a perfect fit with some interference on its contact.

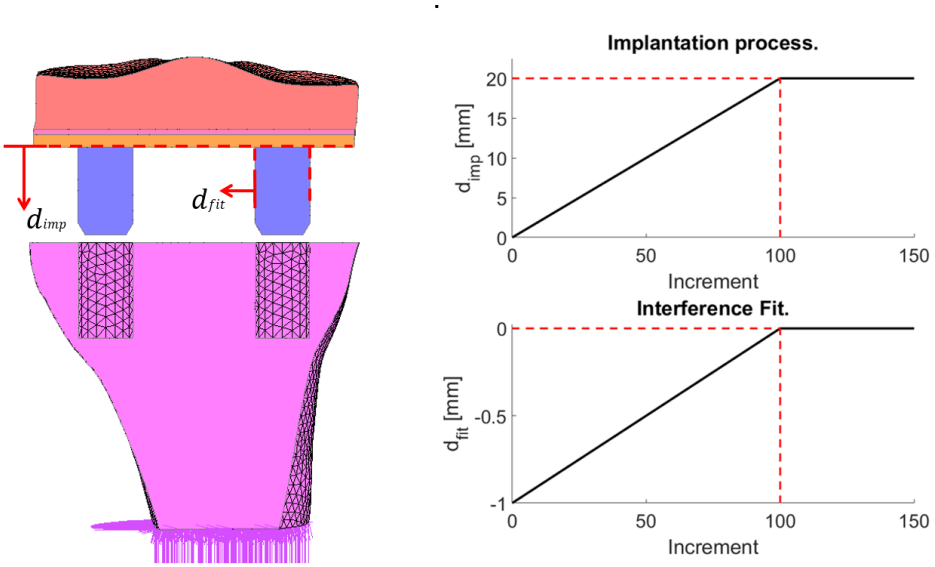

Figure 2.10: Graphical representation of the insertion process with the implantation distance d_{imp}, and the interference fit d_{fit} values applied per increment. To prevent buckling, d_{fit} was applied in the pegs. The insertion process lasted a hundred increments to ensure convergence.

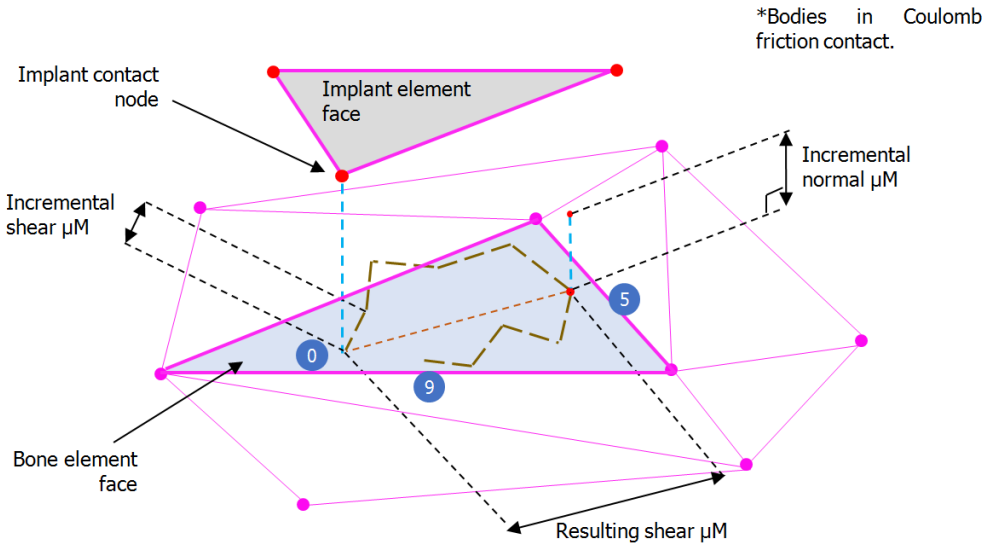

Figure 2.11: Graphical representation of the micromotions algorithm for a hypothetical case of nine increments in the bone-implant contact interface. First, the contact node position is projected into the bone element face during increment (0). Then, the incremental shear and normal micromotions (μM) are tracked for every implant contact node on each increment. By the end of the cycle (increment (9)), the resulting shear micromotions μM are obtained from the longest distance between all the incremental shear micromotions path (e.g. increment (5)).

The previously described process is possible in plastic models because they allow high strains. In the case of an elastic model, implantation is not necessary as the strains should remain below 0.2%. There was no interference fit applied in the linear elastic models, as it is impossible to know which interference fit value would be adequate.

Micromotions algorithm

The micromotion analysis was performed by an in-house made subroutine. It follows the node-face algorithm explained in Van der Ploeg et al. [41] (Figure 2.11). At the beginning of a loading cycle, the contact nodes of the implant with the bone surface are projected onto the closest contact element face of the bone. The projection position is then tracked for each increment, where shear (parallel to the contact surface) and normal (gap) incremental micromotions are obtained. After an activity cycle is finished, the longest shear and gap distances along the total path are obtained. These distances are called resulting micromotions. Tracking occurs for every implant contact node, where a full block diagram of the micromotions subroutine is presented in appendix D.

Once the total shear micromotions have been obtained for each node, the equivalent surface area of that node with respect of the nearest nodes is obtained. This information is used later during each simulation's post-processing. The resulting shear micromotions are compared against a bone ingrowth threshold of 40μm [17, 18]. If a node's micromotions were below the threshold, then ingrowth was assumed for that node. If the micromotions were above threshold, no ingrowth was assumed.

A node was only considered fully ingrown when its shear micromotions were below the threshold for all the activities (Figure 2.12). The ingrowth nodes were multiplied by the total surface area they represented. Individual ingrowth surfaces were summed to obtain the implant total ingrowth surface, which was then divided by the interface area to obtain the extent of ingrowth (in percentage). The mean and standard deviation of the extension of ingrowth was obtained for every density group and each material model.

The results were compared to the retrieval data with the aid of a two one-sided t-test (TOST), commonly named equivalence test [77]. This test shows whether two data sets are significantly equivalent. Contrary to normal t-tests, it is initially assumed that both groups are different. Then, two one sided t-tests are performed with a confidence interval ($CI = 95\%$) approach ($\alpha = 0.05$, $\delta = 5\%$) to observe if the null hypothesis holds true. If the difference between the means with respect to δ is contained within the CI of the experiment ($|\mu_1 - \mu_2| < \delta$), the tests are considered equivalent. If that holds true for this experiment, it means that the simulations of a specific material model are realistic enough to represent Hanzlik et al.'s retrieval data. A second equivalence test was performed for the Persona implant, with the NexGen simulation results as the control group. The second test would give information on how much implant performance changed between both designs, where the Persona is expected to underperform.

Medial tibial collapse algorithm

The second set of simulations consisted of a combination of three plastic material models, ten patients, and two implants to study medial tibial collapse. Implant insertion was performed first to obtain the "realistic" interference fit and to account for implantation softening of the peri-implant surface. Then, the implant was linearly loaded with the stumbling condition in a span of ten increments. After that, the subroutine added 10% of its total BW value for every new increment until collapse was reached. Continuously increasing the stumble load is equivalent to an increasingly worse accident. The chosen body weight of every patient was the mean of Hanzlik et al.'s data (96.81 Kg).

After the load converged in every increment, the positions of the implant's most medial contact node and the most lateral contact node were obtained (Figure 2.13). These were used to calculate the total varus angle. The incremental varus alignment was compared to the collapse threshold of 8° [26]. The simulation stoped when the threshold was reached, as medial tibial collapse has occurred. The simulation was also considered as finished if it crashed due to material instabilities. In that case, the material model was considered incapable of reproducing medial tibial collapse.

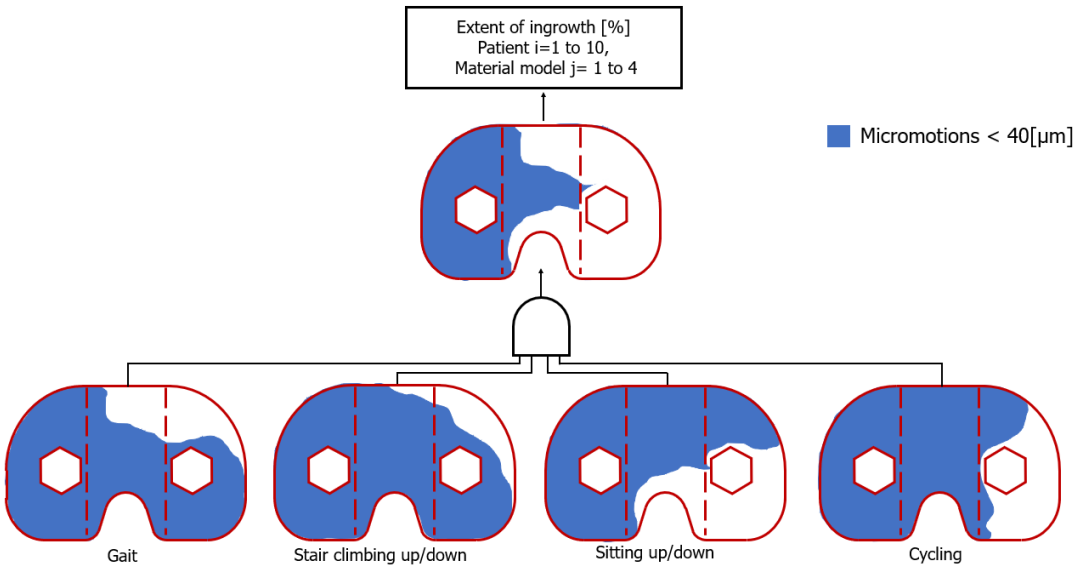

Figure 2.12: Example of the post processing algorithm to combine the ingrowth results for all activities across every patient and material model.

For post-processing, varus alignment was plotted against percentage of body weight under stumbling conditions. The mean and standard deviation were obtained for every density quality of the same material model. The collapse curve of every material model was compared to observe differences in critical instability and failure. Finally, this critical percentage of body weight was compared to the 700% to 900% common stumble threshold (Zimmerman et al. [80]), and to the 5° varus alignment risk threshold (Green et al. [25]). Finally, a medial tibial collapse equivalence test was performed on the Persona implant with the NexGen as control group, similar to the second equivalence test performed in the ingrowth analyses.

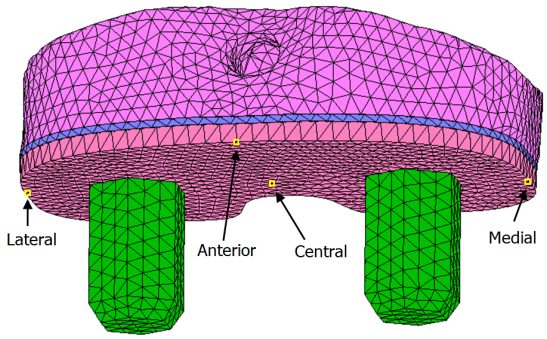

Figure 2.13: Selected nodes for varus alignment measurement within the subroutine. The medial and lateral nodes were used for varus alignment.

3. Results

3.1. Isotropic Crushable Foam model validation

The trabecular cube simulations used to validate the hardening equation showed different behaviour for every material model (Figure 3.1). For the sVM model, the strains were uniformly distributed throughout the cube. For the hICF model, the strains concentrated in areas were the cube density was the lowest. Also, the overall shape of plastic deformation formed a horizontal layer. For the iICF model, the strain concentration in a horizontal line was higher than that observed for the hICF. The plastic strain concentration is also close to the horizontal centre line of the cube, demonstrating the pressure dependency of the ICF plastic models.

For confined test results, the hICF model precisely replicated apparent yield stress at 5% strain (Figure 3.2). A big difference was found in the transition curve between the elastic and the elastoplastic part. The sVM model showed no pressure dependency as expected from the confined test, as it remained almost linear. The iICF model did show yield under confined tests, but was not capable of reproducing the hardening observed in both Kelly et al. data sets. The hICF model was capable of reproducing the hardening behaviour at 5% strain, with almost the same final yield stress when compared with Kelly et al.'s data.

3.2. Material model implantation deformation

For the three plastic models, implantation caused a layer of large plastic strain. These strains allowed the circular drill holes in the bone to adapt to the shape of the implant pegs. Plastic strain concentration differed by material model and by the density quality of the bone. The thickness of the plastic layer was measured to observe the amount of extreme deformations after implantation (Figure 3.3).

The layer of excessive deformations remained relatively constant when the average ash density increased for every material model (Figure 3.4 A-B). Contrary to plastic thickness, the peg's contact stresses were higher for the younger patients (Figure 3.4 D-E). The highest contact stresses and plastic thickness were observed in the sVM model, followed by the hICF model. The iICF model demonstrated the lowest contact stresses and plastic thickness. The NexGen results show a bigger plastic layer (Figure 3.4 C), but the Persona had higher contact stresses (Figure 3.4 F).

After implantation, the shape of the bone adapted differently to the shape of the implant pegs. These changes depend on the material model used (Figure 3.5 A-D). The best adaptation to the implant peg shape was achieved by the iICF model, followed by the hICF model. The sVM model showed the worst adaptation to the implant geometry. The Persona implant showed more surface in contact than the NexGen implant for every material model used (Figure 3.5 E).

3.3. Micromotions and ingrowth analysis

For both implants, different ingrowth patterns occurred when considering different activities and material models (Figures 3.6 and 3.7). The left side of the Figure shows that cycling considers most of the nodes as ingrown for every material model. This is followed by sitting and standing, gait (walking), and finally stair walking. For every material model, the medial posterior side of the implant and around the pegs was estimated to have most bone ingrowth. For gait and stair walking, the anterior side demonstrated almost no ingrowth in both the NexGen and Persona.

For the NexGen results, the extent of ingrowth estimated for the tray was $34.34 \pm 16.71\%$ when using a LE model, $11.84 \pm 4.10\%$ for a sVM model, $29.85 \pm 3.52\%$ for the hICF model, and $42.83 \pm 4.88\%$ for the iICF model. For the pegs, the extent of ingrowth was $10.98 \pm 0.86\%$ for the LE model, $51.14 \pm 7.21\%$ for the sVM, $63.83 \pm 0.71\%$ for the hICF model, and $65.26 \pm 0.92\%$ for the iICF (Figure 3.8 A). When comparing the results with retrieval data from Hanzlik et al. [75], three out of four models overestimate ingrowth in the tray (Figure 3.9 A). Here, the equivalence test results fell into the right side of the CI,

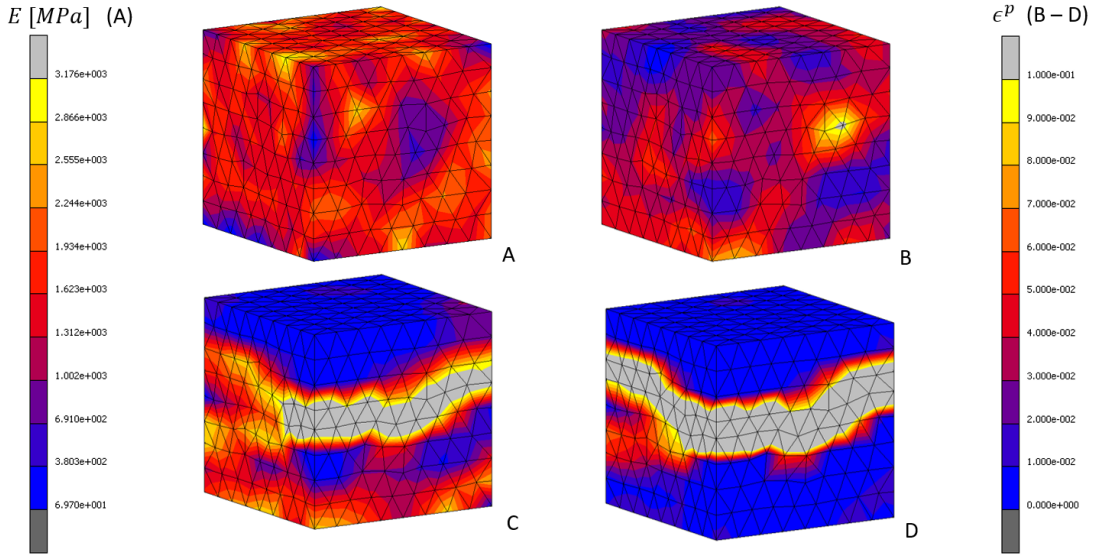

Figure 3.1: Total equivalent plastic strain for the validation cubes for every plastic material model under confined compression. Excessive strains (light grey) were considered beyond 10% as a measure on how much the strains concentrate. A) The Young's Modulus values of the cube. B) Results for the Von Mises softening (sVM) criterion. C) Results of the hardening isotropic crushable foam (hICF) model. D) Results of the ideal isotropic crushable foam (iICF) model.

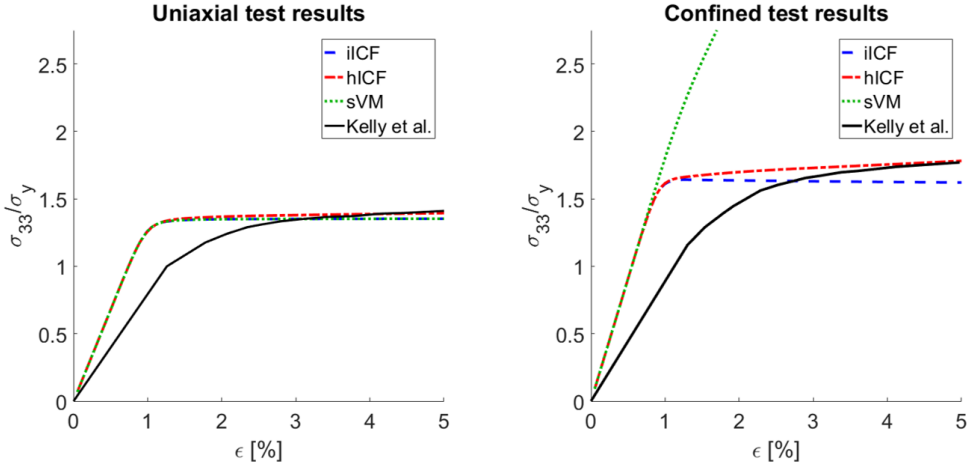

Figure 3.2: Hardening equation validation results for uniaxial and confined stress tests. In black, the ICF curve obtained from Kelly et al. [54]; in red, the curve of the hardening ICF model; in green, the curve for a Von Mises ideal model based on Keyak et al.'s [50] uniaxial yield stress; in blue, the ideal ICF model results.

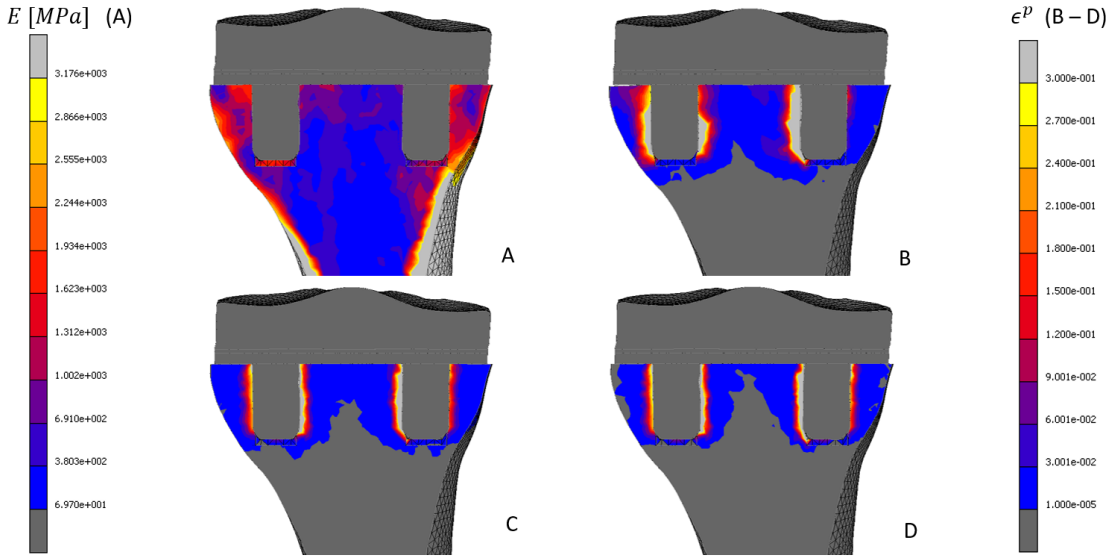

Figure 3.3: Total equivalent plastic strain after implantation. A) The Young's Modulus values of the cube. B) Results for the Von Mises softening (sVM) criterion. C) Results for the hardening isotropic crushable foam (hICF) model. D) Results for the ideal isotropic crushable foam (iICF) model.

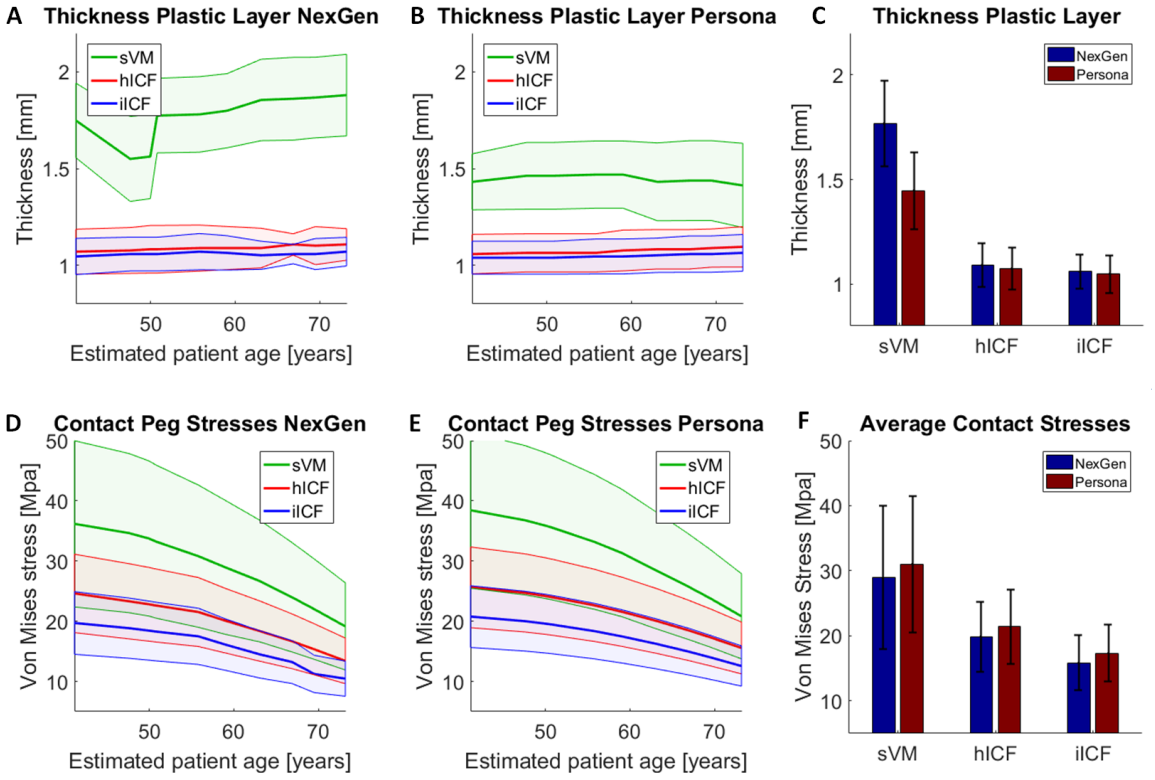

Figure 3.4: A-B) Thickness of plasticity layers around the implants for all the different bone densities and material models. C) Comparison of thickness between implants across all density groups. D-E) Average contact stresses around the pegs, which represent the average fixation stresses between the implant and the bone for each material model. F) Comparison of contact stresses between implants across all density groups.

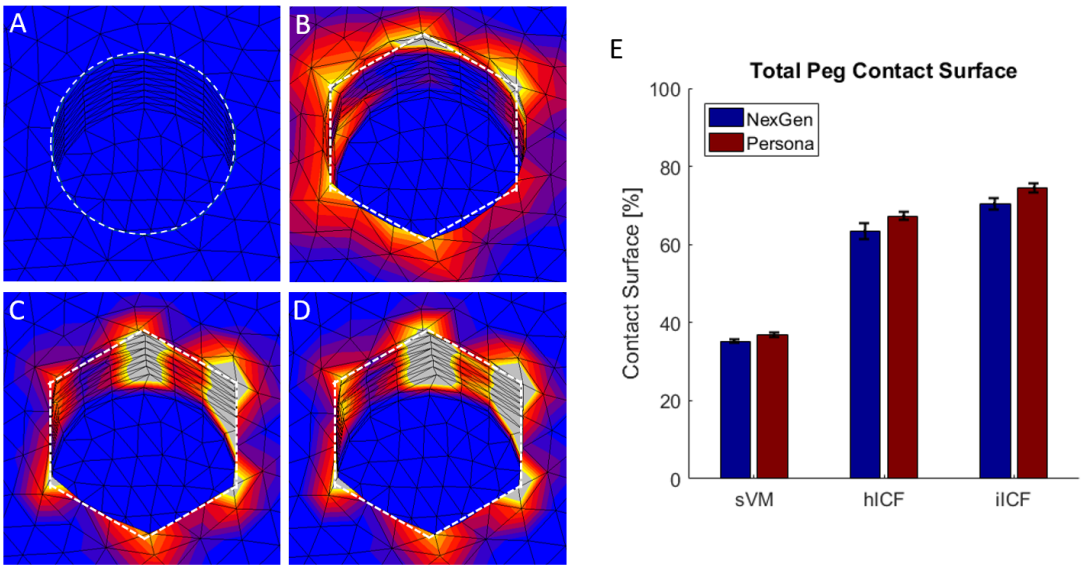

Figure 3.5: Total equivalent plastic strain plot of the shape of the bone peg holes after implantation in every material model used. A) Original drill shape before implantation. B) sVM model post-implantation shape. C) hICF post-implantation shape. D) iICF post-implantation shape. E) Percentage of implant peg surface in contact with the bone after insertion between both implants.

which means the simulations overestimated ingrowth. Also for the tray, the sVM model under-predicted the ingrowth results, as its equivalence test values fell to the left of the CI. For the pegs, both ICF models over-predicted ingrowth. The sVM model was the most accurate in predicting peg ingrowth, but it cannot be considered equivalent to the retrieval data, as its equivalence test values fall outside the CI. The LE model under-predicted peg ingrowth the most, as the equivalence test results were far left from the CI.

When dividing the tray area in medial, lateral, and central zones, the NexGen implant showed a different pattern of ingrowth than the retrieval data (Figure 3.8 C). According to Hanzlik et al. [75], the medial, lateral, and central zones should have almost the same ingrowth, with a slight increase in the medial side. All the material models used showed a different pattern of ingrowth. The medial ingrowth is overestimated when compared to the central and lateral side in every model. The iICF also overestimates the lateral side. A similar pattern emerges for the Persona implant (Figure 3.8 D). No micromotions higher than $150\mu m$ were observed in any experiment. Also, the highest shear strains observed were in the order of 2.17%.

When comparing the NexGen with the Persona implant (Figure 3.8 B), the estimated overall bone ingrowth surface of the NexGen was $25.04 \pm 10.8\%$ when using a LE model, $27.49 \pm 4.43\%$ with a sVM model, $43.38 \pm 2.67\%$ with a hICF model, and $51.76 \pm 3.09\%$ when considering an iICF model. In the case of the Persona implant, the estimated bone ingrowth surface was $36.06 \pm 1.59\%$ for the LE model, $27.17 \pm 4.19\%$ for the sVM model, $44.77 \pm 4.18\%$ for the hICF, and $54.17 \pm 4.22\%$ for the iICF model. The Persona implant performed better than the NexGen in three out of four material models. The NexGen implant only performed better when using a SVM model. According to the equivalence test between implant performance (Figure 3.9 B), the Persona was only significantly better than the NexGen when using a LE model. When using any plastic material model, both implants were found significantly equivalent, without apparent improvement between designs.

3.4. Medial tibial collapse

For every sVM simulation, the total equivalent plastic strain was more dispersed in the surroundings of the medial peg compared to the hICF model at the point of collapse (Figure 3.10). For the sVM results, plastic strains can be observed 2 cm below the medial peg, reaching until the cortical bone of the most medial side. For the hICF model, the strains were concentrated around and below the peg

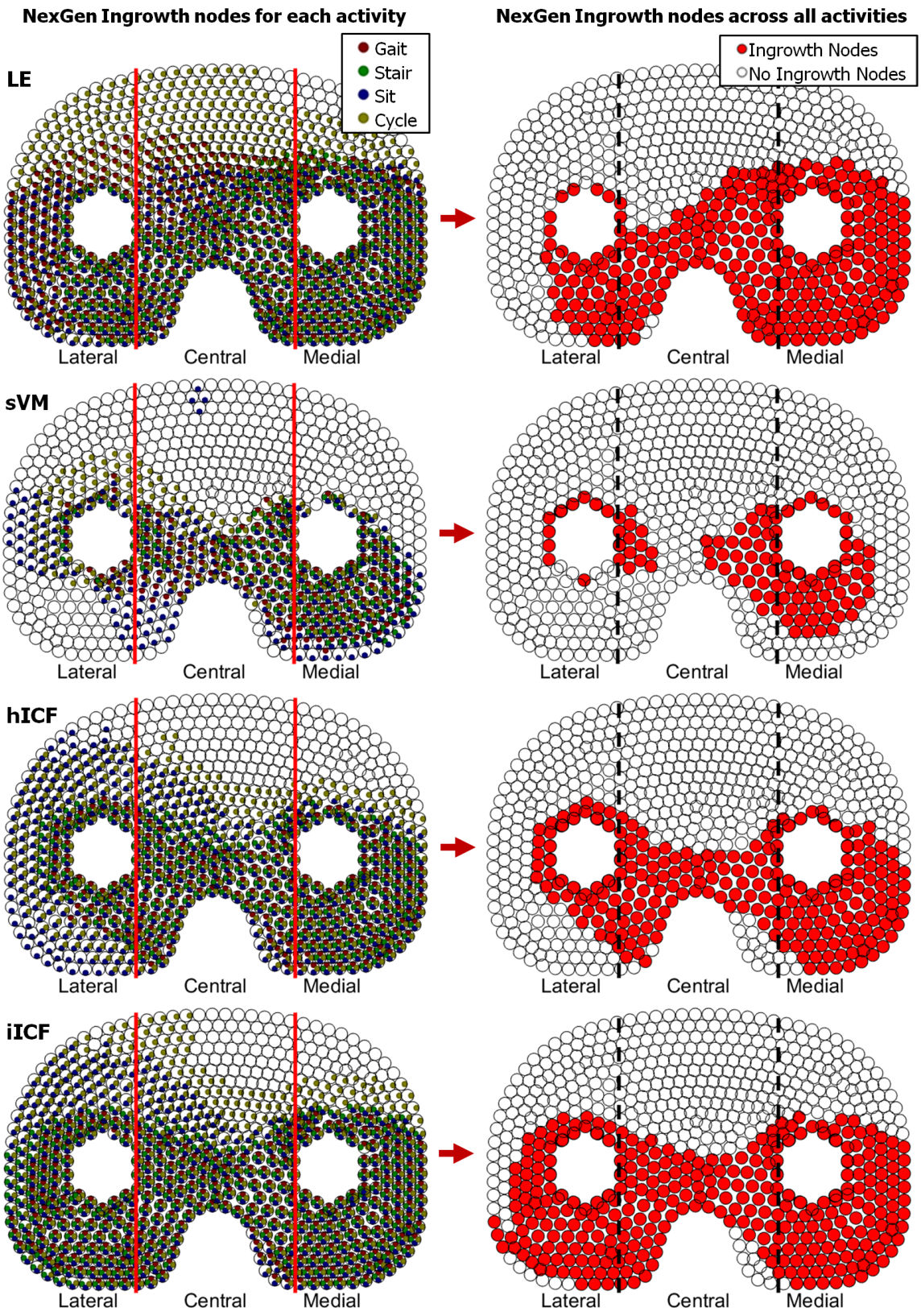

Figure 3.6: Bone ingrowth for every activity and the total ingrowth in every material model for NexGen implant and the bone with the lowest density quality. Left: Ingrowth contact nodes (coloured) for every activity. Right: Final ingrowth nodes after activity combination. (LE = Linear Elastic; sVM= softening Von Mises; hICF= hardening Isotropic Crushable Foam; iICF= ideal Isotropic Crushable Foam.)

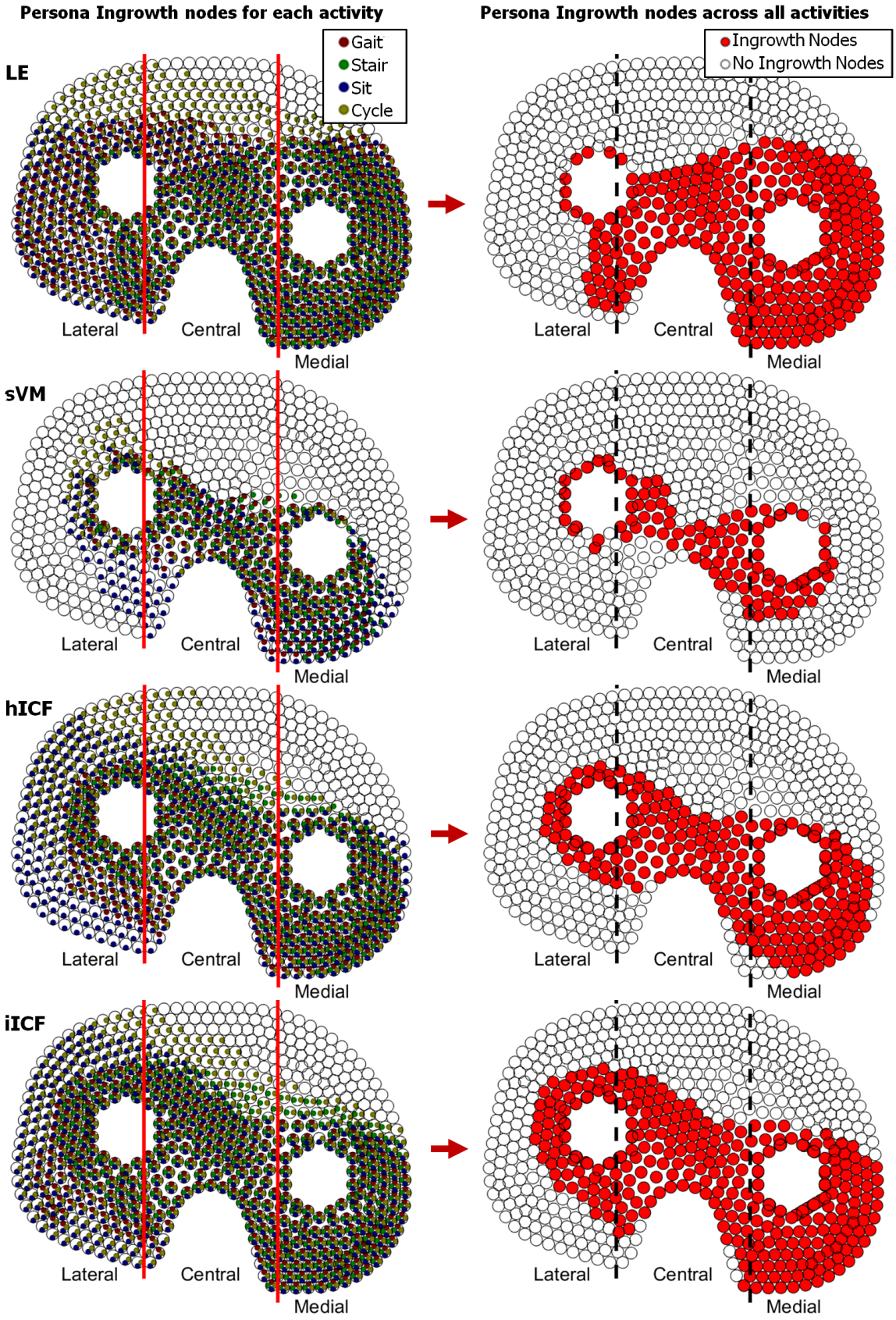

Figure 3.7: Bone ingrowth for every activity and the total ingrowth in every material model for Persona implant and the bone with the lowest density quality. Left: Ingrowth contact nodes (coloured) for every activity. Right: Final ingrowth nodes after activity combination. (LE = Linear Elastic; sVM= softening Von Mises; hICF= hardening Isotropic Crushable Foam; iICF= ideal Isotropic Crushable Foam.)

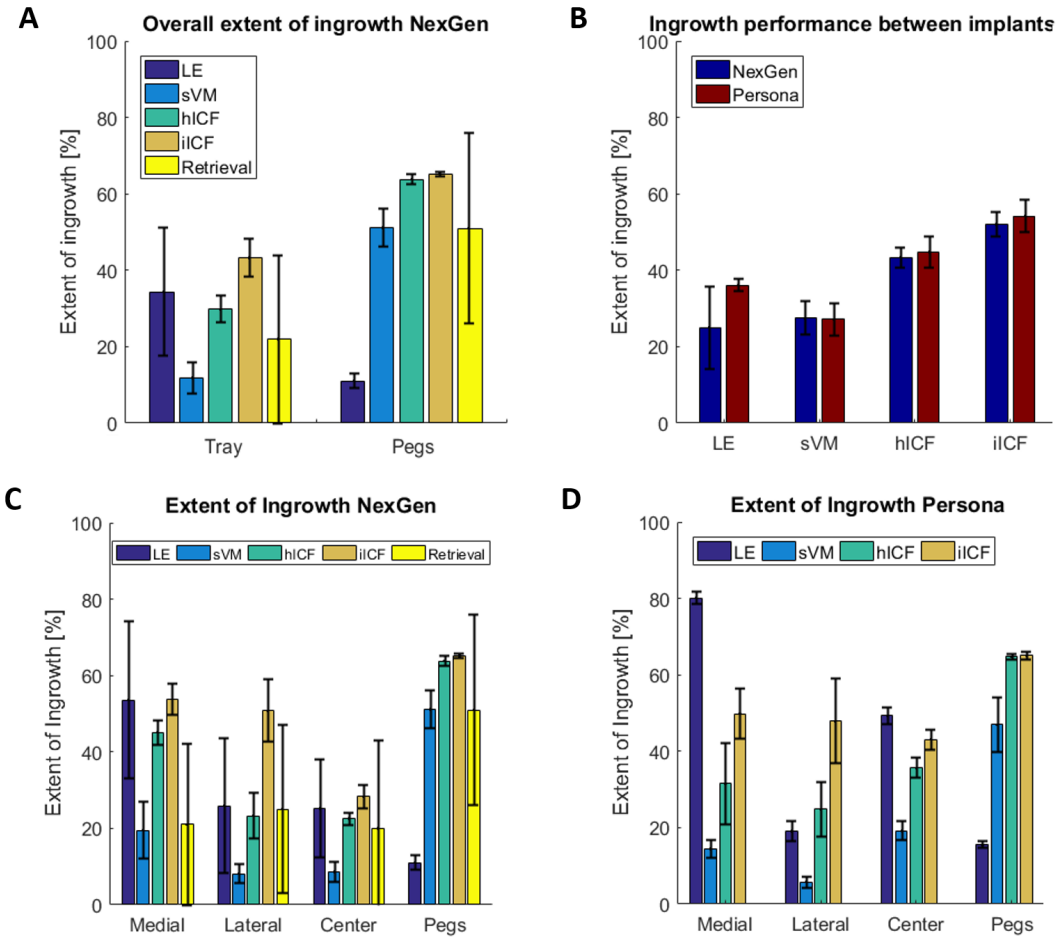

Figure 3.8: A) Extension of ingrowth (EoI) of the NexGen implant compared to material model used and retrieval data obtained from Hanzlik et al. [75]. B) EoI of the Persona and NexGen implants between material model. C) EoI of the NexGen for all surface areas, where medial, lateral and center are tray regions. D) EoI of the Persona for all surface areas, where medial, lateral and center are tray regions. (LE = Linear Elastic; sVM= softening Von Mises; hICF= hardening Isotropic Crushable Foam; iICF= ideal Isotropic Crushable Foam.)

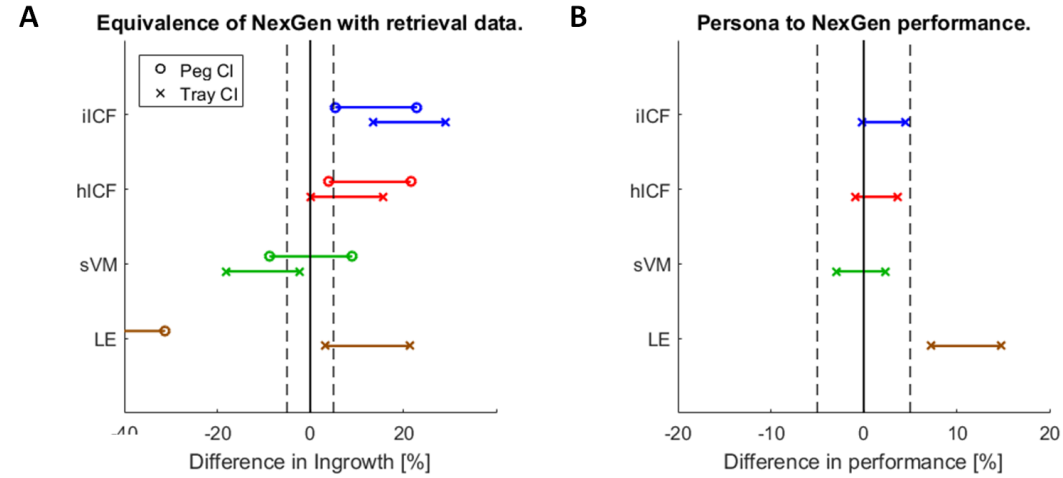

Figure 3.9: A) Confidence interval (CI) of the equivalence test between the simulations and the retrieval data by material model and implant region. B) Equivalence test between the implants performance. Positive difference in performance means that the Persona outperformed the NexGen.

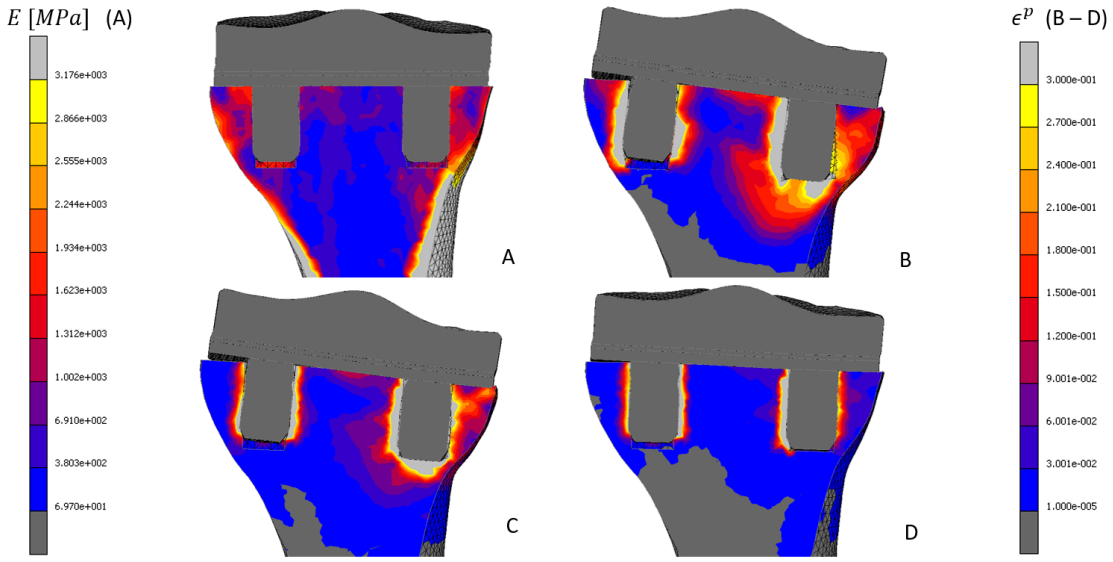

Figure 3.10: Front plane section of three different final results for medial tibial collapse. A) The Young's Modulus values of the bone. B) Equivalent plastic strain ϵ^p results for the Von Mises softening (sVM). C) ϵ^p results for the hardening isotropic crushable foam (hICF). D) ϵ^p results for the ideal isotropic crushable foam (iICF) model.

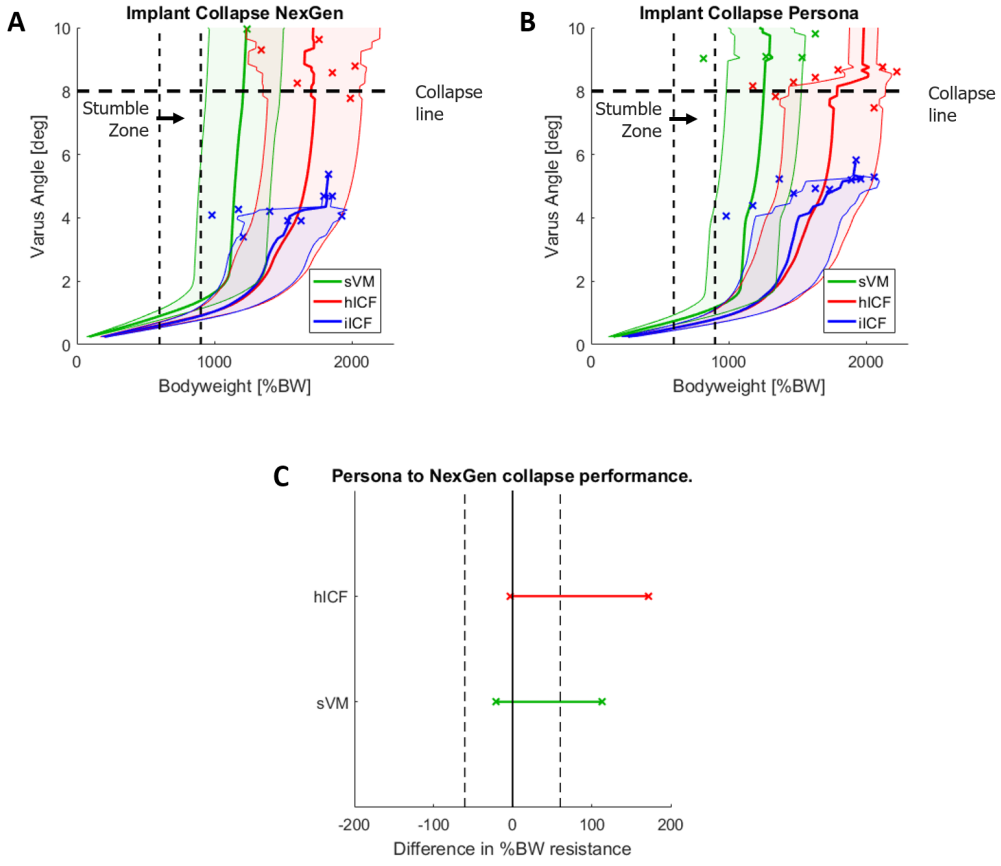

Figure 3.11: A) Mean collapse curves for the NexGen implant for each material model, shaded area shows standard deviation. B) Mean collapse curves for the Persona implant for each material model, shaded area shows standard deviation. C) Persona's medial tibial collapse equivalence test results with the NexGen simulations as control group. (sVM= softening Von Mises; hICF= hardening Isotropic Crushable Foam; iICF= ideal Isotropic Crushable Foam.)

while reaching the collapse angle of 8° without material instabilities, as intended. Lateral side lift-off was present in every simulation of the sVM and hICF model. No simulation converged to collapse for the iICF, as material instabilities appeared before reaching the collapse threshold.

A varus angle of 8° was used as a threshold for medial tibial collapse. Not every simulation converged until the desired collapse angle (Figures 3.11 A and B) as several simulations resulted in inside-out elements. No simulation presented inside-out elements for the sVM model, while three simulations presented inside-out elements for the hICF model, and twenty (all) simulations for the iICF model.

For the NexGen, the average percentage of body weight at collapse was $1209\%BW \pm 268.1$ for the sVM model simulations and $1729\%BW \pm 343.2$ for the hICF. It is unknown for the iICF, as none of the simulations was able to reach the collapse threshold. For the Persona, the average percentage of body weight of collapse was $1251\%BW \pm 272.3$ for the sVM model simulations and $1737\%BW \pm 420.8$ for the hICF. Just as in the NexGen iICF simulations, the values for the Persona iICF simulations are unknown. For every material model, sudden structural instabilities occurred at different points.

The iICF model showed a higher decline in structural instability when compared to the hICF model, as the curves behaved similarly prior to the structural instability. The equivalence test between the implants (Figure 3.11 C) determined an almost equivalent performance between the implant designs. The Persona slightly over-performed the NexGen implant design, but not enough to be considered significantly different.

4. Discussion

4.1. Validation of hardening function for the ICF model

Both the uniaxial and confined yield stress tests adequately fit the experiment from Kelly et al. [54] at 5% strain when using a hICF model (Figure 3.2). Differences observed in the linear part of the curves are due to a different choice for Young's Modulus in the current study. The current study used the ash density equations from Keyak et al., which lead to an average Young's Modulus for the cube of 5.2 MPa. In contrast, Kelly et al. simply considered a Young's modulus of 4 MPa for the trabecular bone cube.

The cube validation tests help to explain the main difference between the Von Mises and the isotropic crushable foam criteria. Under confined compression, the Von Mises criterion is not capable to account for changes in pressure, as it draws a line that extends almost linearly. A similar situation occurs under implantation conditions, where the shear to pressure ratio R is around 1.26. To compare, under uniaxial conditions $R = 3$, and lowers to $R = 0.92$ under confined stress conditions, meaning that implantation conditions are more related to confined compression than uniaxial compression. On the other hand, the crushable foam model demonstrates adequate yielding in both uniaxial and confined tests. The fact that plastic strains distribute around the whole cube when using the sVM criterion is also explained by its lack of pressure dependence (Figure 3.1), as only changes in shape led to yield. This is especially clear in both ICF model cube results. Here, the concentration of strains in a horizontal line shows how yielding occurs in the areas with more concentration of pressure and low Young's modulus.

Kelly et al. performed several tests to obtain the necessary information to create a phenomenologically based hardening equation. The development of the present hardening equation seems to be a good approach when experimental data is not available. The hardening behaviour may be represented by an equation that updates ash density after yield when permanent changes in bone volume occur, as presented in this study. These validation results also indicate that human and bovine trabecular yielding behaviour may not be so different. Still, more experiments on tri-axial testing machines are necessary to develop a bone-specific material model.

4.2. Implantation analysis

Depending on which material model was used, the bone adapted differently to the implant after insertion. Bone adaptation and total contact was best in the iICF model. This is due to the pressure dependence that caused the shear softening effect (Figure 2.8). Also, the fact that the yield surface does not grow means there will be higher volumetric plastic strains. This allows plastic strains to remain concentrated around the closest bone elements (Figure 3.3), allowing the bone to adapt better to the implant pegs. When adding the hardening function, the shear softening effect dissipates as the yield surface grows (Figure 2.8 bottom). This caused the contact stresses to rise, so that the plastic strain dissipated in more elements surrounding the pegs. Strain dissipation reduced material instability risk while still adapting to the implant shape. The biggest difference was observed when using a sVM model (Figure 3.4 A), as the sVM model is incapable to account for hydrostatic pressure, plastic strain will only occur by shear deformations (changes in the element shape). This effect can explain why the average thickness in plasticity almost doubles the pressure dependent models. Also, as the conditions are mostly confined, softening does not occur. This increases contact stresses and distributes more into the surrounding elements, and shape adaptation is limited.

Kelly et al.'s [54] indentation tests on bovine trabecular bone showed that at approximately 2 mm of indentation a white layer of bone is formed. This layer has approximately the same thickness as the indentation and is formed of plasticised bone. In the current study, the metal and bone overlap 0.89 mm in the corners of the hexagon. This causes a plastic layer of about 1.2 mm for the hICF, 1.1 mm for the iICF, and 1.4 mm for the sVM model. Thus, the iICF model seems to be a good candidate to predict plasticity around cementless implants, as its plastic layer thickness was the closest to the amount of peg overlap. These claims still have to be validated with experimental data, as there is

no characterised ICF model for the human tibia yet. The use of the ν_p and K values from a bovine trabeculae should not invalidate these experiments as the compressive yield strength between them only varies by 2.96% [55].

The contact stresses for the hICF model were higher than those of the iICF model, suggesting that the hardening function may be overestimating the yield surface growth. This makes sense, as the consideration for hardening only takes into account the decrease of volume during compression, but not the micro structure changes of the trabecular bone. Currently there is no limit on how much the yield surface can grow for the hICF model. Regarding trabecular bone, if the yield surface grows as density increases, the porosity should decrease. Then, the yield growth under compression should end when porosity reaches zero, as density changes are not possible anymore. The growth limit of the yield surface may be controlled by a total free surface function, similar to the one used in the SED remodelling theory from Weinans et al. [88]. Implementing a free surface function could be performed in a future study, as adding this variable into the current study would have required more time than available.

The implantation process is affected by several limitations. First, the implant was inserted with a negative interference fit, which was linearly reduced during the insertion process. This is equivalent to priorly shrinking the implant peg and slowly expanding it back to its original shape during insertion. In reality, no implant peg would be capable to shrink before being inserted. Nevertheless, this consideration is necessary for the simulation to avoid excessive bone flexion. This would result in too much buckling, material instabilities, and simulation crashing. A more realistic simulation would be to just push the implant into the bone. This would then scratch the bone such that small particles fall below the peg. However, modelling the falling particles would require remeshing in every iteration with elements of the same size as the bone particles. The latter is almost impossible, as small mesh elements make it very hard to work with plastic material models. Not considering falling particles may result in an over-prediction of contact surface and stresses. This especially holds true for the sVM model, which requires shear deformations to soften the elements.

Another limitation of the model might be using displacement boundary conditions instead of forces for insertion. This means that the insertion of the pegs was simulated as a constant movement, whereas in reality it is hammered into place by the surgeon. As such, using displacement boundary conditions does not take into account vibrations and possible hammering mistakes by the surgeon. However, as no study that correlates hammering forces during insertion was found, it was necessary to use displacement boundary conditions. Simulating insertion using forces would make it possible to account for small alignment errors and vibrations. This would reduce the over-estimation of contact surface and softening around the bone. Such a study could correlate the required average insertion force with the average bone ash density, while accounting for small variations of insertion angle and impact conditions. This could further improve future FEM analyses.

4.3. Micromotions and ingrowth analysis

For every material model, the activity that prevented ingrowth the most was stair walking (Figure 3.6). The lack of ingrowth was caused by high micromotions on the lateral and anterior sides of the implant. These high micromotions derived from high peak normal forces that were accompanied by high moments (Figures A.2 and A.2). When high forces and moments combine, the final load tilts toward the medial posterior side of the implant, explaining why most ingrowth is concentrated in this area. When using gait loads, the same load distribution towards the medial posterior side of the implant is observed. However, only one peak force with moments tilts the implant towards the medial posterior side, which is the reason why gait is the load that prevents ingrowth the second most.

Cycling and sitting/standing up had an overall higher extension of ingrowth than gait and stair walking. A possible explanation for this is that the peak normal forces in these activities are lower than in gait and stair walking. For both activities, the extension of ingrowth was higher on the lateral side, with no ingrowth on the anterior side. Both cases were accompanied by higher moments towards the lateral side of the implant (positive moment in z-axis). For cycling and sitting/standing up, the final loads tilted

towards the lateral side, which was the area with higher ingrowth. As most ingrowth occurs where the final normal forces are higher, the ingrowth pattern seems to be determined by the highest peak force and the direction of the moments in that peak.

The lack of anterior ingrowth for every activity may be due to the positioning of the pegs. These are located on the posterior side of the implant tray. There, they provide anchor points for all forces and prevent movement. The anterior side, however, is unprotected against flexion, leading to more micromotions. The lack of anterior ingrowth could be prevented by an extra design feature, like the anterior boss nub of the modular version of the Monoblock implant [89]. Another possibility to promote anterior ingrowth is to modify the insert surface. This would improve implant kinematics, allowing loads to better distribute around the tray, and lead to a better ingrowth distribution.

Differences in bone ingrowth around the tray and pegs for both implants and all material models were observed (Figures 3.8 C and D). For the pegs, when using a LE model, the ingrowth prediction around the pegs lies below the standard deviation of the retrieval data (Figure 3.9 A). Here, the peg ingrowth prediction for the LE model was far left of the confidence interval of the retrieval data. The under-prediction of ingrowth for the LE model can be explained by the lack of contact stresses and interference fit in the pegs. Simulating a realistic interference fit for a heterogeneous LE model is difficult because contact stresses would have to be higher than most elements' yield stress values. This would complicate the analysis and lead to unreliable results.

The use of plastic material models, on the other hand, leads to a more accurate prediction of ingrowth when compared to the retrieval data. The average ingrowth of every plastic material model stayed within the standard deviation of the retrieval data. The better prediction of plastic material models is due to their capability to simulate more realistic contact stresses, as they are obtained from high strain interference fits. Both ICF models slightly over-predicted ingrowth beyond the confidence interval of the retrieval data. The over-prediction might derive from the implantation algorithm, as this does not account for bone loss and scratch during implant insertion. The sVM model seems to most adequately predict ingrowth around the pegs. This might derive from the way in which the bone behaves when using an sVM model, as the bone mesh does not adapt well to the shape of the implant peg. This results in low surface contact between the bone and the implant, which compensates for the lack of bone loss due to insertion scratching. Less surface contact increases the total micromotions around the pegs, leading to a better prediction of ingrowth when comparing to the ICF models.

Comparing bone ingrowth around the tray of the NexGen with the retrieval data shows that the hICF model predicts ingrowth most accurately, as it is closest to the mean of the retrieval data and almost within the confidence interval of the equivalence tests (Figure 3.9 A). The model's hardening effect and pressure dependence cause both moderate contact stresses and surface contact between the implant and the bone. This results in a slight over-prediction of the level of ingrowth, but very similar to that of the retrieval data. The sVM model slightly under-predicted the amount of bone ingrowth. This can be explained by a lack of total surface contact, which leads to a higher tilting of the implant tray. The use of an iICF model leads to an over-prediction of ingrowth beyond the standard deviation of the previous two models. This might derive from high amounts of surface contact. Next to material model and used loads, micromotion results also seem to be greatly affected by total surface contact as well as press-fit conditions.

None of the material models was capable to replicate the same ingrowth pattern as observed in the retrieval data. There, the extension of ingrowth was evenly distributed around the three tray regions. The simulations, however, predicted more ingrowth on the medial side of the tray than in central and lateral regions. This uneven distribution of ingrowth around the tray might be due to the activities that were selected for this study. As stated above, the loads that caused the least ingrowth were gait and stair walking. These activities have concentrated forces and moments towards the medial and posterior side, leading to an uneven distribution of ingrowth. The use of implant-specific musculoskeletal models to obtain activity loads might be required to accurately predict the pattern of ingrowth around the tray. This is necessary because the shape of the insert plays a big role in load distribution.

The lack of significant equivalence of the results with the retrieval data might derive from different reasons. To start, the statistical power of the retrieval data was rather low, as it only consisted of 32 bones. This makes it less reliable to be used as validation data. Further, the retrieval data derives from deceased patients who have had their implants for an average of three years without revision, where effects such as repeated cycles of ingrowth, implant migration, or remodelling might have occurred. However, these effects are of no interest for the current study, as the focus lies on early ingrowth effects within the first few weeks, and in how far ingrowth is affected by implant insertion and material models. Normally, shear strains should also be considered when simulating bone ingrowth, which were left out from the current study as it focuses on micromotions. Additionally, the current study showed peaks of shear strains of 2.17% around the implant tray, which is bellow the differentiation threshold of 3.75% found by Lacroix et al. [90]. Thus, it was not necessary to consider them, as they did not affect the results.

According to the equivalence tests results for the Persona performance (Figure 3.9 B), the Persona showed a significantly better performance than the NexGen when using a LE model. These results suggest that the Persona outperforms the NexGen and should thus be placed into the market. When using any plastic material model, the difference in performance between the implants becomes less obvious. The equivalence tests show that both implants are significantly equivalent when using a plastic material model. A reason for this might be the higher medial surface area of the Persona, compared to the NexGen. A higher area means less total stresses and micromotions around the tray, and therefore more ingrowth. Also, the medial peg of the Persona is set more posteriorly than that of the NexGen, and therefore closer to the point towards which the loads tilt (as they also tilt towards the medial and posterior side of the implant). This posterior peg of the Persona presents a pivot point for the loads to dissipate. These peak loads do not dissipate when a plastic material model is used, as the contact stresses are higher due to the interference fit. For the Persona, these high contact stresses might balance the geometrical advantages of having a medial peg. Therefore, the amount of micromotions for the Persona and the NexGen is approximately equal.

Adding extra considerations to the material model, like viscoelasticity, damage, or migration tracking may lead to better results for the NexGen than the Persona. Also, implant-specific kinematics may show less differences between the implants, as the Persona and NexGen geometries differ. The insertion method of the implants might also negatively affect their performance. The NexGen is inserted by simply hammering the implant into the bone, just as any other tibial component, whereas a special tibial inserter is used for the insertion of the Persona. This inserter might twist the bone when released from the insert, damaging its initial fixation. This potentially dangerous situation is shown as a warning sign on page six in the insertion manual of the Persona implant [83]. Adding the effects of such an accident to the implantation process of the simulations might result in lower performance of the Persona compared to the NexGen.

4.4. Medial tibial collapse analysis

For the current study, a simple stumble load was applied until the bone collapsed, representing a catastrophic collapse accident. Although no study was found that assessed medial collapse, the results of the current study present several important observations regarding the material model used for simulating the phenomenon. For the sVM model, the strains at collapse are spread around the implant such that they reach the cortical bone area below, increasing the tensile stresses of the cortical bone elements beyond their yield. Cortical bone yielding should be studied more accurately with a crack model, rather than a compression deformation model like sVM. Additionally, the sVM curve collapses very close to Zimmerman et al.'s stumble region (Figure 3.11). This should not occur, as the knee would not collapse after a simple stumble case of 900 %BW. This suggests that the sVM model might not be adequate to represent medial tibial collapse.

Contrary to the sVM model, the ICF models might show too much overall body-weight while maintaining a low varus angle. Using an iICF model is problematic for medial collapse analysis, as the FEM algorithm shows too many material instabilities. As discussed above, these material instabilities are caused by high concentrations of plastic strain and inside-out elements. Further, it is impossible to account for

the changes in density around every element when bone is crushed without a hardening equation. This should cause higher contact stresses and dissipate plastic strains, protecting against material instabilities. Then, the hardening of the contact elements appears to provide a computational method that prevents material instabilities. Additionally, the hICF model also provides protection against structural instabilities, as its collapse slope was less prominent that the one of the iICF and the sVM.

Hardening does not have a limit for density changes, as density should stop increasing when porosity reaches zero. Any porous structure that is compressed enough will eventually become non-porous. As discussed in the implantation section, a free surface area function might be used to limit density growth. This has been applied in SED remodelling based functions from Huiskes et al. [38]. Further, implementing a free surface area function into hardening would automatically distinguish between cortical and trabecular bone in the equations, making a density threshold for trabecular and cortical bone unnecessary. This limit of hardening may also reduce the potentially unrealistic contact stresses that the hICF model predicts between the bone and the implant.

The previous observation leads to a future hypothesis. The SED remodelling theory from Huiskes et al. considers only elastic behaviour. To be able to study a cementless implant, it is necessary to understand how plastic SED could affect remodelling. The change of density of every element under volumetric plastic strains could be taken into account for a remodelling analysis in cementless models. This could be explained by the fact that density already changes when using a pressure dependent plastic model. The stiffness of an element could be immediately updated when it becomes plastic, just as when it is updated by the elastic SED values. This would allow to perform remodelling experiments in cementless implants while maintaining considerations of early interference fit resulting from insertion.

A simple experiment to corroborate the medial tibial collapse findings of the current study might be performed with post-mortem bone samples. Several post-mortem bone specimens must be implanted with NexGen implants. Then, the implanted bones must be loaded in the stumbling conditions specified in this study until collapse. Afterwards, an anterior transverse cut should be performed in the centre of the implant pegs to measure whitening zones of the implant. The whitening plastic zone could then be correlated to the plasticity thickness areas obtained in the results of this project. These could give information about which material model predicts medial collapse better. Given the time and budget available for this project, it was not possible to perform these experiments. The medial collapse results show that there are many differences between the bone behaviour under extreme conditions, which should be taken into account during the design of new implants. Further analysis on applied material models should be performed.

5. Conclusions

It seems that the developed hardening function for an ICF model is capable to predict hardening adequately. This is because the function predicted the same final yield stress present in Kelly et al.'s data. This function was applied to micromotions as well as medial collapse simulations. The hICF model is promising for medial tibial collapse future analyses, as it does not show fatal material instabilities and does not fail close to the stumble thresholds as a sVM model. Also, the results of tray ingrowth of the hICF model were more equivalent to the retrieval data than those of any other model. Further, it is necessary to fully validate the hardening function with tri-axial tests on bone specimens. For this, it is also suggested to validate a function which limits hardening yield surface growth with a free surface area function.

Simulating implantation was demonstrated to be necessary prior to analysis, as the implantation output provides the adequate press-fit stresses and surface contact required for the implant to remain stable. Also, implantation appears to be an adequate indicator of the validity of the plastic model, as the concentrated plasticity around the implant changes depending on the material model used, just as the contact stresses of the cementless implant. Physical experiments in which an implant is inserted and then cut through a specific plane to obtain whitening zones is necessary to validate more realistic simulations of contact stresses.

Light activities such as cycling and squatting (activity similar to sitting/standing up) are recommended as they show high levels of ingrowth when analysed separately. The results suggest that stair walking should definitely be avoided, as it was the activity that caused the least ingrowth. Although gait also led to lack of ingrowth, it is an activity that cannot be restrained from the patient. However, it is suggested to walk as little as possible during the early stages after surgery, and certainly not to carry heavy loads. Tests on implant-specific loads obtained from musculoskeletal models should be used in future studies, as they might provide an ingrowth pattern that correlates better with retrieval data.

Micromotion experiments on simple specimens would provide information on the accuracy of the predicted micromotions, revealing which material model most accurately predicts micromotions. Further, the bone ingrowth results from every material models were not fully validated with the retrieval data. Extra considerations, like migration, iterative ingrowth, shear strains, and remodelling might eventually make the simulations significantly equivalent to retrieval data. Additionally, a bigger population is required for a retrieval study to have the adequate power for it to be used as validation data. Overall, the results of the sVM and the hICF models were the closest to be equivalent to the retrieval data. The sVM model slightly under-predicted the data, while the hICF model slightly over-predicted it.

To accurately simulate medial tibial collapse, future experiments need to include migration tracking and adequate use of a remodelling subroutine. Nevertheless, progress was achieved in the current study, as differences in collapse behaviour and instabilities were observed when using different plastic material models. For future research, it is suggested to include plasticity into remodelling by updating density after plastic volumetric changes, which is possible only when using pressure dependent models. Physical tests similar to those suggested for implantation should be performed to observe the total distribution of whitening areas after collapse. This data should also be used to correlate the respective model with the experimental collapse results.

The ingrowth simulations were not capable to accurately predict that the Persona implant would fail compared to the NexGen. When only using a LE model, the Persona implant was expected to outperform the NexGen. But when adding complexity into the material model, the results show that the performance may not be as good as expected. Complexity such as non-linear plasticity and pressure dependent bone models are enough to tell that the NexGen and Persona implants are equivalent in performance, and should have gone through more iterations before being placed into the market. More experiments and variables have to be considered before obtaining a realistic model that can predict the Persona failure.

6. Acknowledgements

I want to thank Nijmegen's Orthopaedic research lab and its staff members for supporting and guiding me during my internship, literature review, and thesis project, including Nico Verdonschot, Dennis Janssen, and Thomas Anijs. Additionally, I want to thank my TU Delft supervisor Amir Zadpoor and Mohammad Mirzaali for reviewing and commenting on my literature review and thesis. I specially want to thank Natascha Roos for helping me with the thesis' grammar and style. Finally, I want to thank my friends and family who have supported me throughout my academic and personal life.

A. Input loads for micromotion experiments.

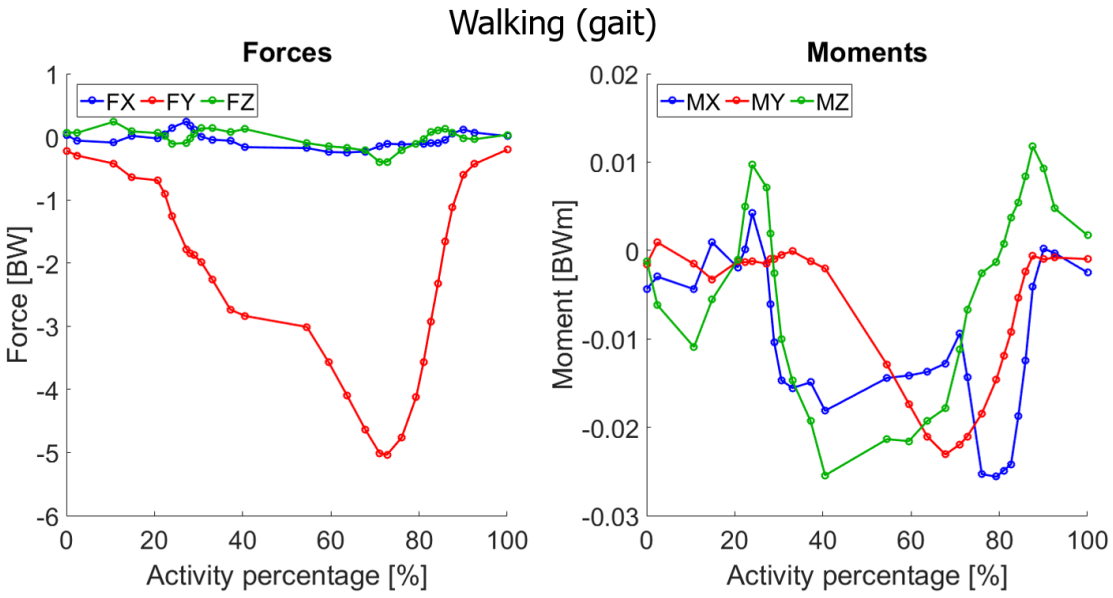

Figure A.1: Loading conditions for gait analysis, obtained from Bergmann et al. (2008) [44]. The original data was filtered so only changes of less than 10% in the main load and moment directions would remain, decreasing the amount of increments from 121 to 30.

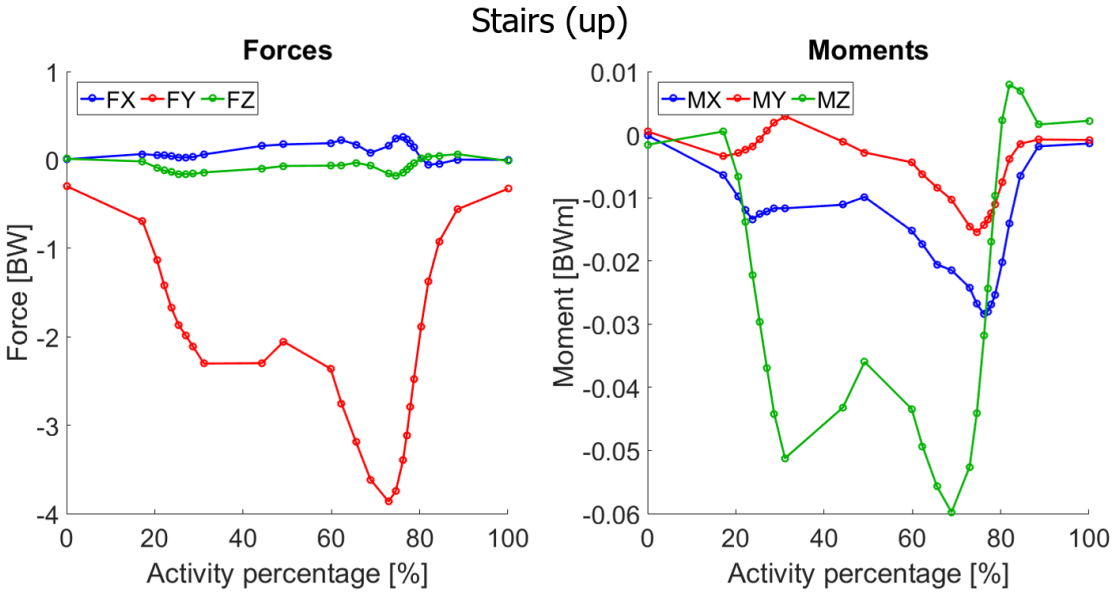

Figure A.2: Loading conditions for stair climbing analysis, obtained from Bergmann et al. (2008) [44]. The original data was filtered so only changes of less than 10% in the main load and moment directions would remain, decreasing the amount of increments from 129 to 25. These data points were combined with downstairs walk.

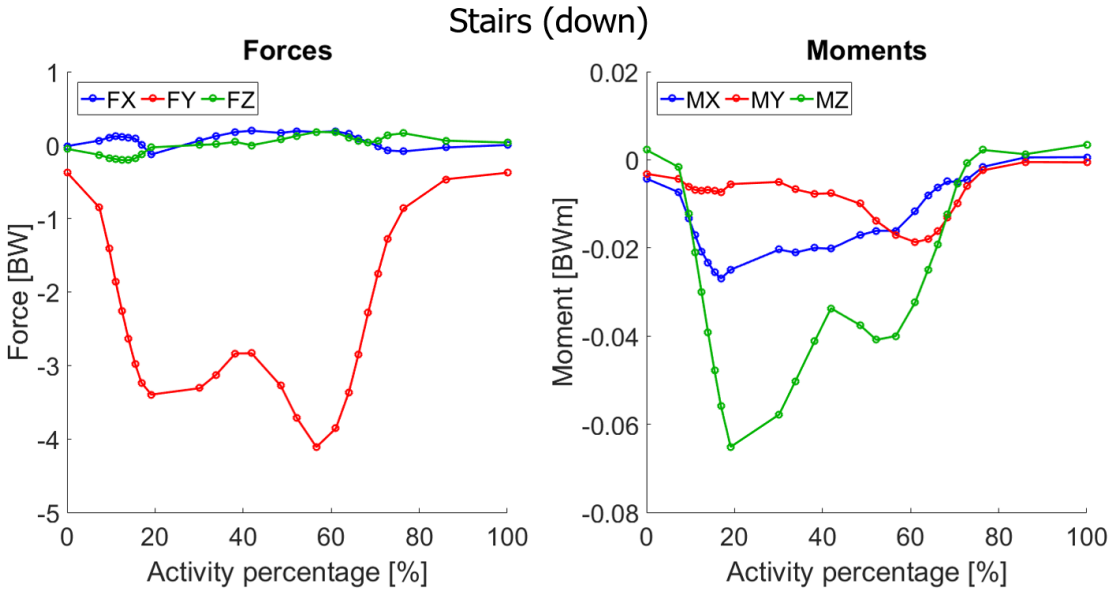

Figure A.3: Loading conditions for walking downstairs analysis, obtained from Bergmann et al. (2008) [44]. The original data was filtered so only changes of less than 10% in the main load and moment directions would remain, decreasing the amount of increments from 129 to 26. These data points were combined with stair climbing.

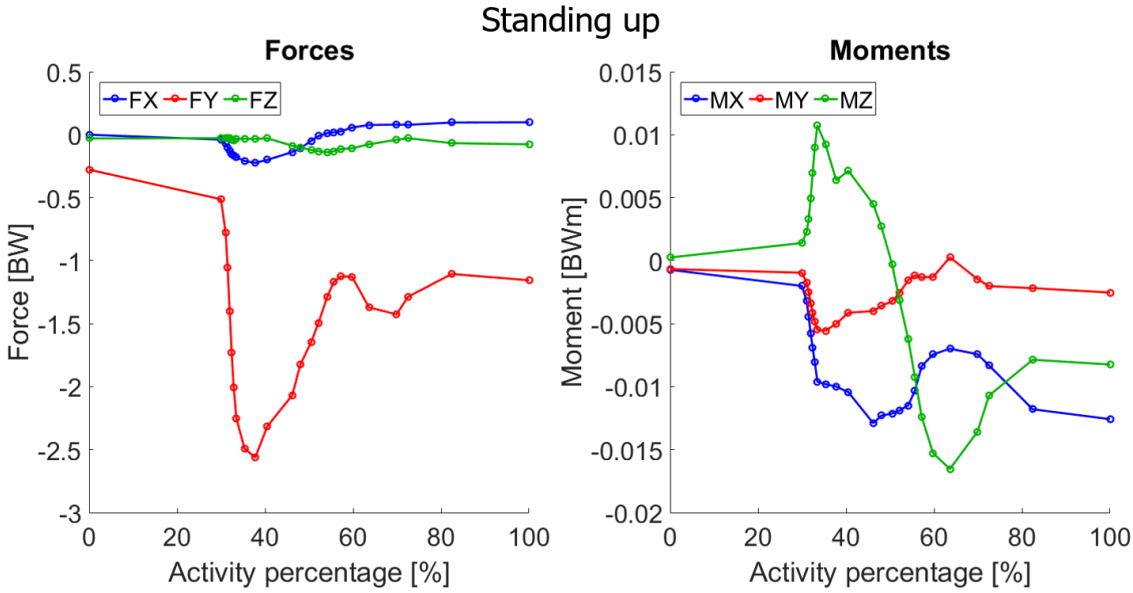

Figure A.4: Loading conditions for standing up analysis, obtained from Bergmann et al. (2008) [44]. The original data was filtered so only changes of less than 10% in the main load and moment directions would remain, decreasing the amount of increments from 672 to 23. These data points were combined with sitting down.

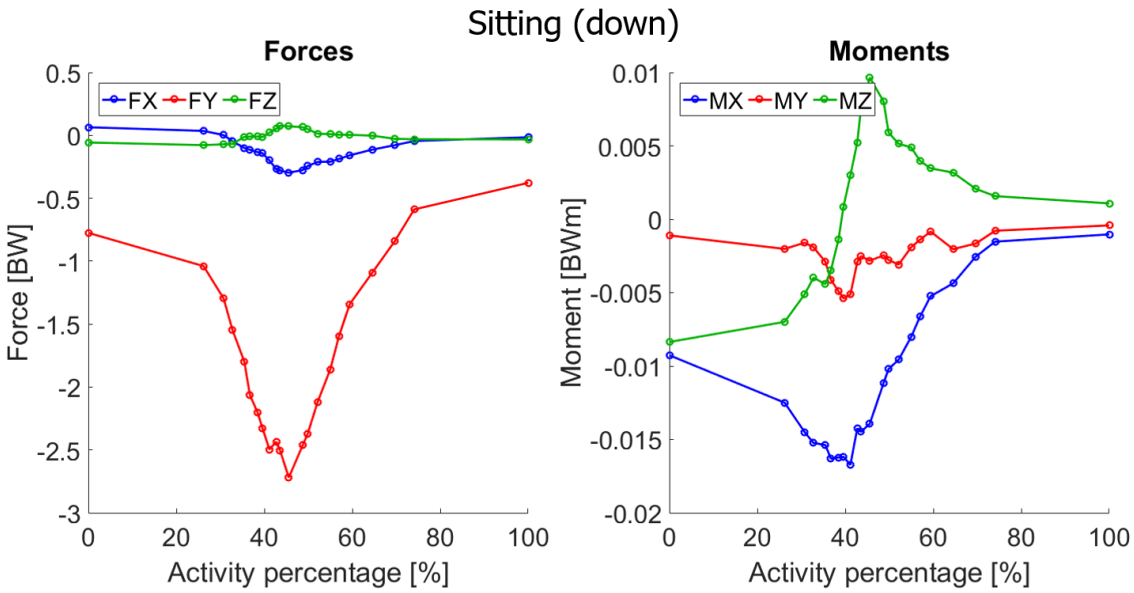

Figure A.5: Loading conditions for sitting down analysis, obtained from Bergmann et al. (2008) [44]. The original data was filtered so only changes of less than 10% in the main load and moment directions would remain, decreasing the amount of increments from 672 to 23. These data points were combined with standing up.

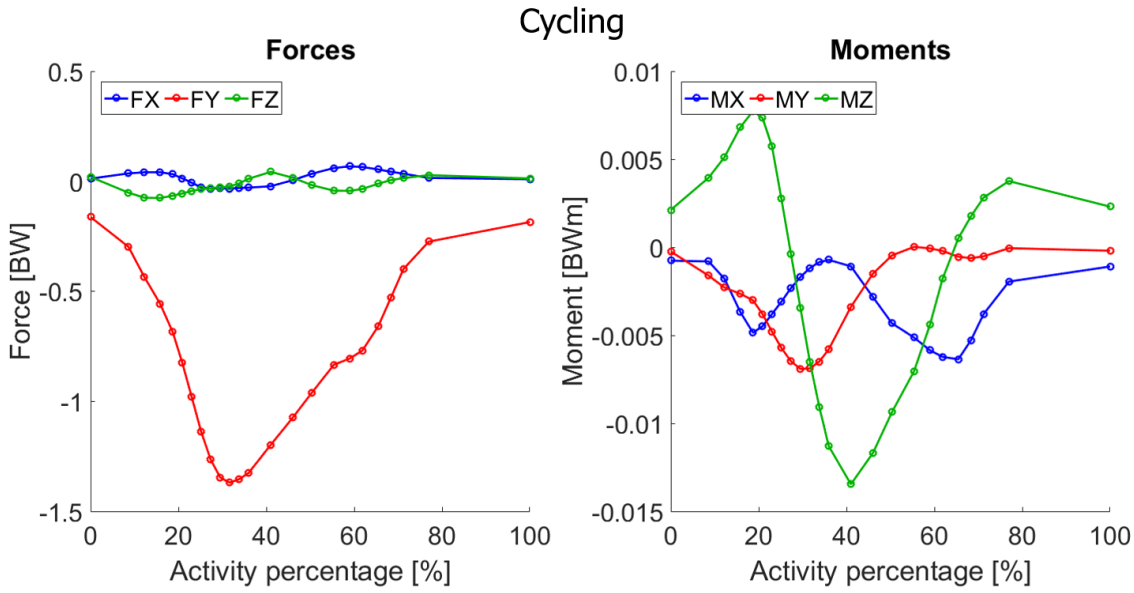

Figure A.6: Loading conditions for cycling analysis, obtained from Bergmann et al. (2008) [44]. The original data was filtered so only changes of less than 10% in the main load and moment directions would remain, decreasing the amount of increments from 139 to 24.

B. Isotropic Crushable Foam model hardening function demonstration.

The yield criterion of the isotropic crushing foam model (f_{ICF}) was originally developed by Deshpande and Fleck (2000) [87], who defined its ellipse shaped surface as:

$$f_{ICF} = \sqrt{q^2 + \alpha^2 p^2} - q_y \tag{B.1}$$

Where q is the equivalent Von Mises stress (second invariant of the deviatoric stress tensor $\overline{\overline{S}}$) and p is the hydrostatic pressure (first invariant of the stress tensor $\overline{\overline{\sigma}}$). α is the ellipse shape constant, and q_y the yield stress in pure shear. These are defined as:

$$q = J_2 = \sqrt{\frac{3}{2}\overline{\overline{S}} : \overline{\overline{S}}} = \sqrt{\frac{1}{2}[(\sigma_{11} - \sigma_{22})^2 + (\sigma_{22} - \sigma_{33})^2 + (\sigma_{33} - \sigma_{11})^2 + 6(\sigma_{12}^2 + \sigma_{13}^2 + \sigma_{23})]} \tag{B.2}$$

$$p = I_1 = -\frac{1}{3} trace(\overline{\overline{\sigma}}) = -\frac{1}{3}(\sigma_{11} + \sigma_{22} + \sigma_{33}) \tag{B.3}$$

$$\alpha = \frac{3K}{\sqrt{9 - K^2}}; \qquad K = \frac{\sigma_{yo}}{p_{yo}} \tag{B.4}$$

$$q_y = \sigma_y \sqrt{1 + (\frac{\alpha}{3})^2} \tag{B.5}$$

$$\sigma_{yo} = c\rho_{ash_o}^d \tag{B.6}$$

K is the initial ellipse shape parameter, p_{yo} the initial yield under pure hydrostatic pressure, σ_{yo} the initial yield stress in uniaxial loading, ρ_{ash_o} the bone's initial ash density, and c and d its exponential regression constants obtained from Keyak et al (2003)[50]. Also, a Von Mises to hydrostatic pressure ratio R defined as:

$$R = \frac{q}{p} \tag{B.7}$$

All the previous parameters define the geometry of the ICF model yield surface in the pq plane. A graphical representation of this can be seen in figure B.1.

Additionally, Kelly et al. (2012) [53] considers a non-associative flow rule for trabecular bone. For that, the flow potential rule g_{ICF} was defined as:

$$g_{ICF} = \sqrt{q^2 + \beta^2 p^2} \tag{B.8}$$

Where β is the ellipse shape constant for the flow potential rule, defined by the plastic Poisson's ratio ν_p as:

$$\beta = \frac{3}{\sqrt{2}} \sqrt{\frac{1 - 2\nu_p}{1 + \nu_p}} \tag{B.9}$$

According to the flow rule, plastic flow occurs when the yield criterion reaches zero $f_{ICF} = 0$ [91]. Then, the stress rate vector $\dot{\overline{\sigma}}$ for non-associative materials is be defined as:

$$\dot{\overline{\sigma}} = [\overline{\overline{D_e}} - \frac{\overline{\overline{D_e}}\,\overline{m}\overline{n}^T\overline{\overline{D_e}}}{h + \overline{n}^T\overline{\overline{D_e}}\,\overline{m}}]\dot{\epsilon} \tag{B.10}$$

With $\overline{\overline{D_e}}$ the elastic stiffness matrix, $\overline{m} = \frac{\partial g_{ICF}}{\partial \overline{\sigma}}$ the direction of plastic flow, $\overline{n}^T = \frac{\partial f_{ICF}}{\partial \overline{\sigma}}^T$ the transposed gradient vector of the yield function, $\dot{\epsilon}$ the strain rate, and h the hardening function.

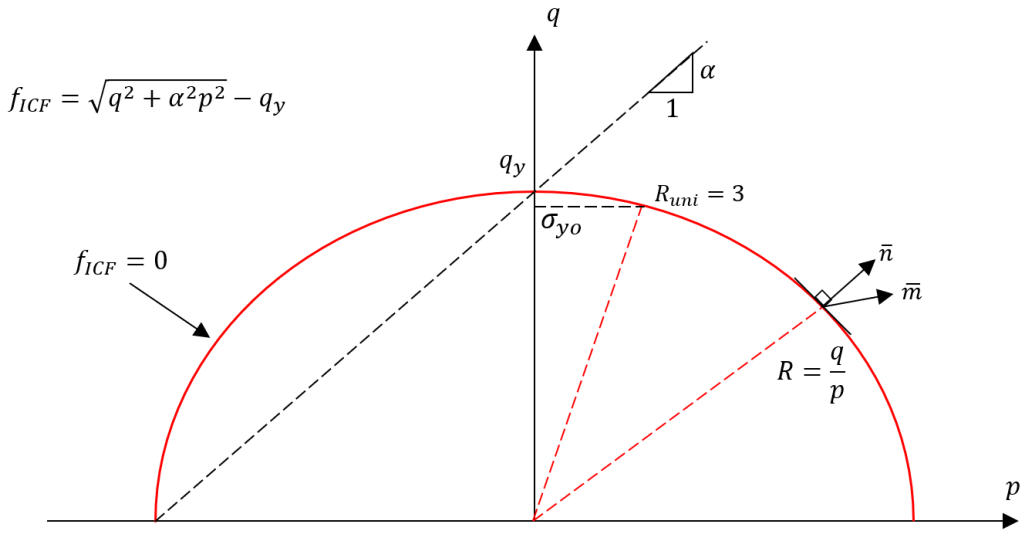

Figure B.1: Graphical representation of the isometric crushing foam model yield criterion. The yield surface in the pq plane is represented by an ellipse. The equivalent Von Mises yield strength q_y depends on the Von Mises to hydrostatic pressure ratio R. The loading configuration becomes uniaxial when $R = 3$, which means the current equivalent yield stress becomes the uniaxial yield stress ($q_f = \sigma_y$).

The hardening function usually depends on the hardening parameter κ which depends on the yield criterion f. This function can be defined as [91]:

$$h = -\frac{1}{\dot{\lambda}} \frac{\partial f_{ICF}}{\partial \kappa} \dot{\kappa} \tag{B.11}$$

Where $\dot{\lambda}$ is the magnitude of plastic flow, and $\dot{\kappa}$ is the hardening rate. If a work hardening condition is considered, which means:

$$\dot{\kappa} = \frac{1}{\sigma_y} \bar{\sigma}^T \dot{\bar{\epsilon}} \quad \text{or} \quad \dot{\kappa} = \frac{q_y}{\sigma_y} \dot{\epsilon}^p \tag{B.12}$$

And considering that the plastic strain rate $\dot{\bar{\epsilon}}$ is defined according to the flow rule:

$$\dot{\bar{\epsilon}}^p = \dot{\lambda} \bar{m}, \tag{B.13}$$

The following expression for the hardening function h can be obtained:

$$h = \frac{-1}{\sigma_y} \frac{\partial f_{ICF}}{\partial \kappa} \bar{\sigma}^T \bar{m} \tag{B.14}$$

Now, to simplify the previous equation, it is necessary to first extend the direction of plastic flow:

$$\bar{m} = \frac{\partial g_{ICF}}{\partial \bar{\sigma}} = \frac{1}{2\sqrt{q^2 + \beta^2 p^2}} \begin{pmatrix} 2\sigma_{11} - \sigma_{22} - \sigma_{33} - (2/3)\beta^2 p \\ 2\sigma_{22} - \sigma_{11} - \sigma_{33} - (2/3)\beta^2 p \\ 2\sigma_{33} - \sigma_{11} - \sigma_{22} - (2/3)\beta^2 p \\ 6\sigma_{12} \\ 6\sigma_{13} \\ 6\sigma_{23} \end{pmatrix} \tag{B.15}$$

And by applying it in equation B.14:

$$\begin{aligned} h = \frac{-1}{2\sigma_y \sqrt{q^2 + \beta^2 p^2}} \frac{\partial f_{ICF}}{\partial \kappa} [\sigma_{11}(2\sigma_{11} - \sigma_{22} - \sigma_{33} - \frac{2}{3}\beta^2 p) + \sigma_{22}(2\sigma_{22} - \sigma_{11} - \sigma_{33} - \frac{2}{3}\beta^2 p) + \\ \sigma_{33}(2\sigma_{33} - \sigma_{11} - \sigma_{22} - \frac{2}{3}\beta^2 p) + 6(\sigma_{12}^2 + \sigma_{13}^2 + \sigma_{23}^2)] \end{aligned} \tag{B.16}$$

Which can be reorganised as:

$$h = \frac{-1}{\sigma_y\sqrt{q^2+\beta^2p^2}}\frac{\partial f_{ICF}}{\partial \kappa}[(\sigma_{11}^2+\sigma_{22}^2+\sigma_{33}^2)-(\sigma_{11}\sigma_{22}+\sigma_{11}\sigma_{33}+\sigma_{22}\sigma_{33})- \frac{1}{3}\beta^2 p(\sigma_{11}+\sigma_{22}+\sigma_{33})+3(\sigma_{12}^2+\sigma_{13}^2+\sigma_{23}^2)] \tag{B.17}$$

And then the previous equation can be simplified by adding the definitions of Von Mises stress B.2, hydrostatic pressure B.3, and flow potential function B.8. It is possible to obtain:

$$h = \frac{-1}{\sigma_y g_{ICF}}\frac{\partial f_{ICF}}{\partial \kappa}[q^2+\beta^2p^2] = -\frac{g_{ICF}}{\sigma_y}\frac{\partial f_{ICF}}{\partial \kappa} \tag{B.18}$$

The change of the yield criterion with respect to the hardening parameter has to be defined. As the equivalent yield stress should be dependent from the hardening parameter $\sigma_y(\kappa)$. When this is applied in the yield criterion B.1, the following is obtained:

$$f_{ICF}(\kappa) = \sqrt{q^2+\alpha^2p^2} - \sigma_y(\kappa)\sqrt{1+(\frac{\alpha}{3})^2} \tag{B.19}$$

When obtaining the derivative with respect of the hardening parameter κ, the following is obtained:

$$\frac{\partial f_{ICF}}{\partial \kappa} = -\frac{\partial \sigma_y(\kappa)}{\partial \kappa}\sqrt{1+(\frac{\alpha}{3})^2} \tag{B.20}$$

Now, as these equations work when the flow rule holds true ($f_{ICF}=0$), the uniaxial yield strength (σ_y) can be written as:

$$\sigma_y = \frac{\sqrt{q^2+\alpha^2p^2}}{\sqrt{1+(\frac{\alpha}{3})^2}} \tag{B.21}$$

Which allows to apply equations B.8 B.20 B.21 into equation B.18:

$$h = \left(1+\left(\frac{\alpha}{3}\right)^2\right)\frac{\sqrt{q^2+\beta^2p^2}}{\sqrt{q^2+\alpha^2p^2}}\frac{\partial \sigma_y(\kappa)}{\partial \kappa} \tag{B.22}$$

Now, adding the definition of the Von Mises to hydrostatic pressure ratio (B.7) to the previous equation to substitute p:

$$h = \left(1+\left(\frac{\alpha}{3}\right)^2\right)\frac{\sqrt{q^2+\beta^2(\frac{q}{R})^2}}{\sqrt{q^2+\alpha^2(\frac{q}{R})^2}}\frac{\partial \sigma_y(\kappa)}{\partial \kappa} \tag{B.23}$$

$$h = \left(1+\left(\frac{\alpha}{3}\right)^2\right)\sqrt{\frac{R^2+\beta^2}{R^2+\alpha^2}}\frac{\partial \sigma_y(\kappa)}{\partial \kappa} \tag{B.24}$$

Now, integrating the work hardening rule when $f_{ICF}=0$ to obtain κ:

$$\kappa = \int \dot{\kappa}\,dt = \int \frac{q_y}{\sigma_y}\dot{\epsilon^p}\,dt \tag{B.25}$$

Where the advantage of choosing a work hardening rule arises, as the normalisation $\frac{q_y}{\sigma_y}$ can be reduced by introducing equation B.5:

$$\kappa = \sqrt{1+\left(\frac{\alpha}{3}\right)^2}\int \dot{\epsilon^p}\,dt \tag{B.26}$$

$$\kappa = \sqrt{1+\left(\frac{\alpha}{3}\right)^2}\epsilon^p \tag{B.27}$$

With this hardening parameter κ, it is possible to obtain the partial differential of both sides of the equation.

$$\partial\kappa = \sqrt{1 + \left(\frac{\alpha}{3}\right)^2}\,\partial\epsilon^p \tag{B.28}$$

Then substitute the hardenig differential $\partial\kappa$ with the equivalent plastic strain differential $\partial\epsilon^p$ in equation B.24:

$$h = \left(1 + \left(\frac{\alpha}{3}\right)^2\right)\sqrt{\frac{R^2+\beta^2}{R^2+\alpha^2}}\,\frac{1}{\sqrt{1+\left(\frac{\alpha}{3}\right)^2}}\,\frac{\partial\sigma_y}{\partial\epsilon^p}, \tag{B.29}$$

Which after reducing, the hardening equation leads to:

$$h = \sqrt{\frac{(R^2+\beta^2)(9+\alpha^2)}{9(R^2+\alpha^2)}}\,\frac{\partial\sigma_y}{\partial\epsilon^p} \tag{B.30}$$

Where the square rooted part of the equation was defined as an incremental hardening constant Ω:

$$\Omega = \sqrt{\frac{(R^2+\beta^2)(9+\alpha^2)}{9(R^2+\alpha^2)}} \tag{B.31}$$

$$h = \Omega\frac{\partial\sigma_y}{\partial\epsilon^p} \tag{B.32}$$

Also, if $\alpha = 0$ and $\beta = 0$ the hardening equation reduces to the common Von Mises hardening definition for metals. In it, the hardening of the material's yield stress depends entirely on the equivalent plastic strain change [91].

Now, the only necessary equation which still needs to be defined is the change of equivalent yield stress with respect to equivalent plastic strain $\frac{\partial\sigma_y}{\partial\epsilon^p}$. To obtain such scalar function, the fundamental assumption comes from the use of the volumetric plastic strain ϵ^p_{vol} as a material density change parameter. Volumetric plastic strain indicates the permanent change in the volume of an element, as thus change of density. Then, it could be used to describe the change of yield stress. This applied to equation B.6:

$$\sigma_y = c\rho^d_{ash} = c\left(\frac{m}{V_o(1+\epsilon^p_{vol})}\right)^d_{ash} \tag{B.33}$$

$$\sigma_y = c\left(\frac{\rho_{ash_o}}{1+\epsilon^p_{vol}}\right)^d \tag{B.34}$$

$$\sigma_y = \frac{\sigma_{yo}}{(1+\epsilon^p_{vol})^d} \tag{B.35}$$

The previous equation accounts for the changes of volume of an element during plastic behaviour, but it still cannot be used in equation B.32. For that, it is necessary to relate equivalent Von Mises plastic strain ϵ^p to volumetric plastic strain ϵ^p_{vol}. To achieve this, it is necessary to refer to equations 12a and 12b from Deshpande and Fleck (2000) [87]:

$$\dot{\epsilon}^p = \frac{\dot{\hat{\epsilon}}}{1+\left(\frac{\alpha}{3}\right)^2}\,\frac{q}{\sigma_y}, \tag{B.36}$$

$$\dot{\epsilon}^p_{vol} = \frac{\alpha^2\dot{\hat{\epsilon}}}{1+\left(\frac{\alpha}{3}\right)^2}\,\frac{p}{\sigma_y}, \tag{B.37}$$

Where $\dot{\hat{\epsilon}}$ is the equivalent strain rate. When dividing equation B.36 over B.37 and simplifying using B.7 it is possible to obtain:

$$\dot{\epsilon}^p = \frac{R}{\alpha^2}\dot{\epsilon}^p_{vol} \tag{B.38}$$

Which yields an expression that relates Von Mises and volumetric strain rates. Now, considering that the model works for small increments, allows to integrate both parts over time in the form:

$$\int \dot{\epsilon^p}\, dt = \frac{R}{\alpha^2} \int \dot{\epsilon}^p_{vol}\, dt \tag{B.39}$$

$$\epsilon^p = \frac{R}{\alpha^2} \epsilon^p_{vol} \tag{B.40}$$

Then, by applying the previous equation into B.35 it is possible to obtain:

$$\sigma_y = \frac{\sigma_{yo}}{(1 + \frac{\alpha^2}{R}\epsilon^p)^d} \tag{B.41}$$

An additional condition is necessary, as hardening behaviour is considered to occur only under compression. In that case, and considering that the equivalent plastic strain ϵ^p is obtained from the second invariant of strain, which is given always positive by the solver. It is necessary to rewrite the previous equation to:

$$\sigma_y = \frac{\sigma_o}{(1 - \frac{\alpha^2}{R}\epsilon^p)^d}; \text{ for } p > 0 \tag{B.42}$$

The previous equation also means that the ICF model will remain under ideal conditions when tension is applied. The previous equation can be partially derived with respect to ϵ^p, from which the following is obtained:

$$\frac{\partial \sigma_y}{\partial \epsilon^p} = \frac{\alpha^2 AB(\rho_{ash})^B}{(R - \alpha^2 \epsilon^p)^{B+1}} \tag{B.43}$$

Having the previous equation is the final requirement to have all the information for equation B.32. Therefore, the final hardening equation applied into the flow rule is:

$$h = \begin{cases} \Omega \dfrac{\alpha^2 d\sigma_{yo}}{(R - \alpha^2 \epsilon^p)^{d+1}} & \text{for} \in \ p \geq 0 \\ 0 & \text{for} \in \ p < 0 \end{cases} \tag{B.44}$$

The equation was applied in Marc mentat into a especial subroutine as the software does not have the material model implemented. The algorithm to create this material model into a FORTRAN based subroutine can be found in the next appendix.

C. Isotropic Crushable Foam model subroutine algorithm

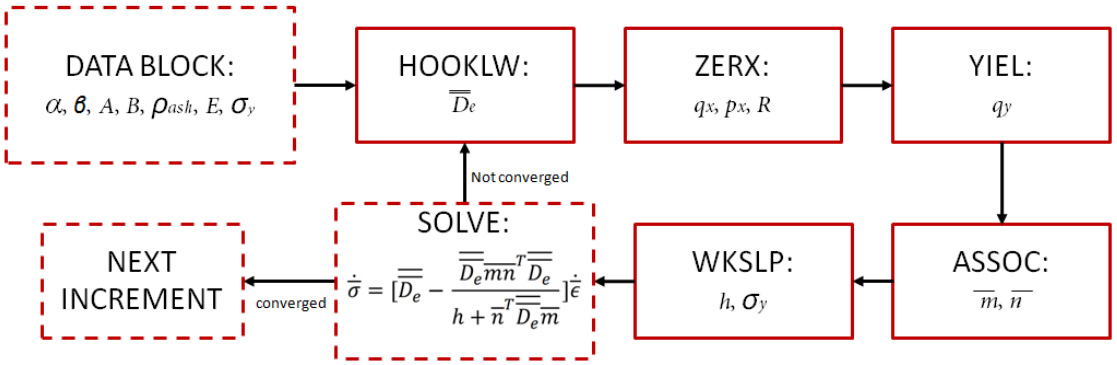

Figure C.1: Block diagram of the isometric crushing foam model yield criterion subroutine. The functions are called for each integration point of each element, where the cycle repeats for each load until the return mapping algorithm converges to the yield surface.

According to Marc 2015 volume D user guide [92], a generalised plasticity model can be defined using five different subroutines (HOOKLW, ZERX, ASSOC, WKSLP, YIEL), each of them involving a specific equation to be solved. The process of each of the subroutines is followed for every increment, and it's called as many times the return mapping algorithm (default solving method for plastic analysis in marc mentat) requires. A simplified block diagram of this sub process is shown in figure C.1.

The first subroutine (HOOKLW), is used in every simulation of this study, and is used to define the bone's heterogeneous properties. As its name implies, it is used to assign the Hooke's law stiffness matrix $\overline{\overline{D}}_e$ constants in terms of each element's Young's modulus E and Poisson's ratio ν. For that, each element's E is calculated from it's ash density ρ_{ash}, based on Keyak et al. (1997) [46] constants.

The second subroutine (ZERX), is used to calculate the current equivalent yield stress (q_f) directly from the stress vector, based on the loading direction R C.2.First the current incremental Von Mises stress (q_x) and the current hydrostatic pressure (p_x) are calculated using equations B.2 and B.3, followed by the ratio R with B.7. The process continues by calculating f_{ICF}. If $f_{ICF} < 0$, yield has not occurred (figure C.2 A), then the yield stress q_f is extrapolated based on the current loading path with the equation:

$$q_f = \frac{R_x q_y}{\sqrt{R_x^2 + \alpha^2}} \tag{C.1}$$

In the yielding case ($f = 0$), the current yield stress is simply defined as the current Von Mises stress $q_f = q_x$ (figure C.2 B). The result of q_f is used to define the equivalent yield stress for every increment in the third subroutine (YIELD).

After calculating q_x, p_x, R and q_f, if yielding is occurring, Marc mentat calls for the (ASSOC) subroutine. This subroutine allows to define the direction of plastic flow $\overline{m}$ (equation B.15). The subroutine requires the flow vector to be multiplied by the current equivalent Von Mises stress $q_x\overline{m}$ as means for later internally normalise the vector. The subroutine is also responsible to internally calculate the gradient

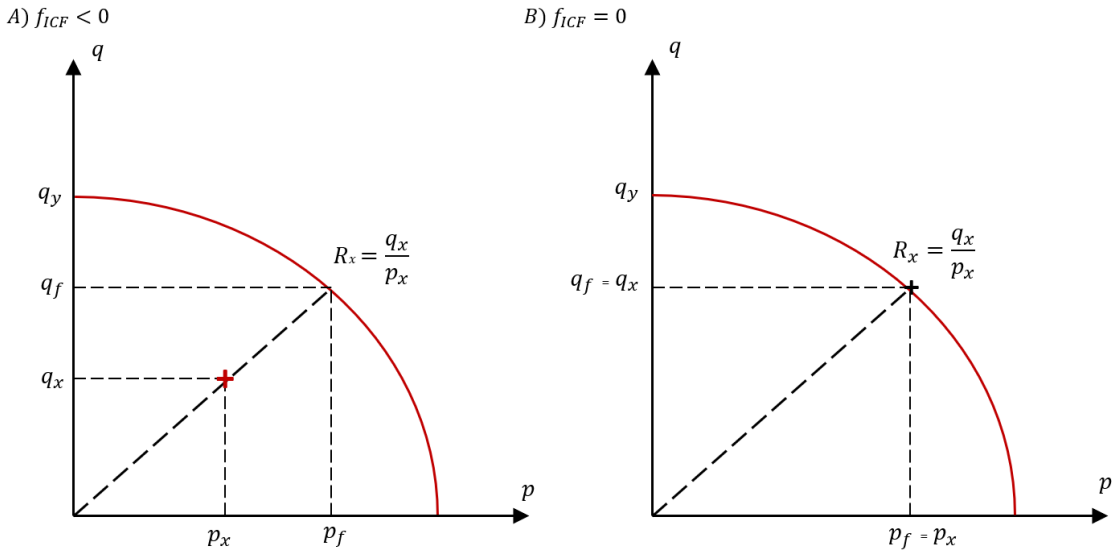

Figure C.2: Case scenarios in which the equivalent yield stress (q_f) is calculated in the ZERX subroutine. A) The subroutine remains in elastic zone and the yield stress is extrapolated based on the current loading path R_x. B) The loading arrived at the yield point, further analysis of stress flow and hardening begin.

of the yield function $\overline{n}$, which is calculated numerically using q_x.

Finally, the subroutine WKSLP is called to define the hardening function h and the new yield surface uniaxial strength σ_y. For that, both values are calculated in terms of the total equivalent plastic strain ϵ^p using the equations B.44 and B.42. The equivalent plastic strain is provided by the subroutine, obtained as a result from the previously defined non-associative flow rule. The constants c, d, α and β are obtained from the data input of the simulation, just as the value of ρ_{ash} of each element.

This process is internally repeated by the subroutine as many times it is necessary for the return mapping algorithm to converge. It is also performed for every integration point of every bone element. This subroutine was validated by repeating the experiments in cubes of trabecular bone performed by Kelly et al. (2013) [54].

D. Micromotions finite element algorithm

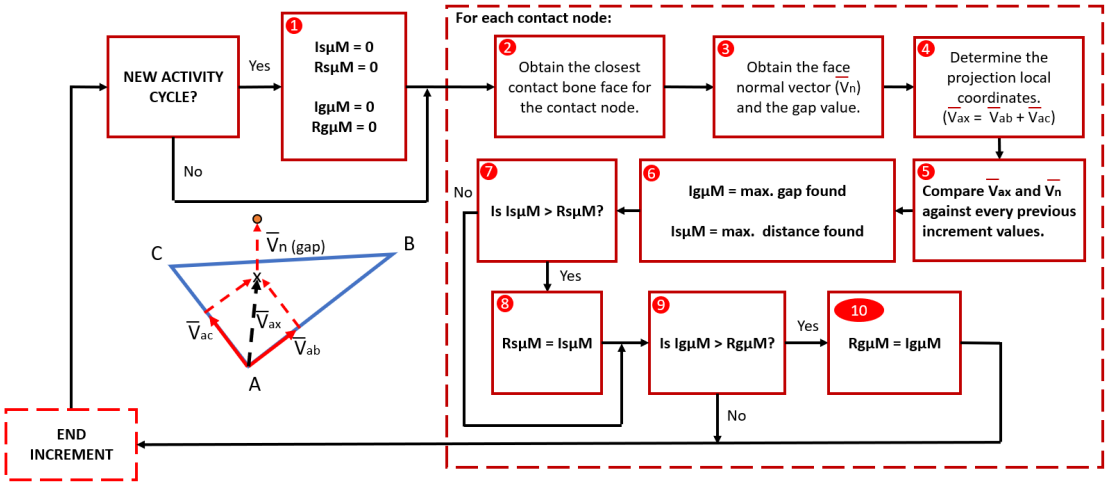

Figure D.1: Block diagram for micromotions analysis for every increment. The analysis is prepared at the beginning of each increment and calculates: incremental shear micromotions ($Is\mu M$), incremental gap micromotions ($Ig\mu M$), resulting shear micromotions ($Rs\mu M$), and resulting gap micromotions ($Rg\mu M$). In the sketch one can observe a representation of a contact node (in orange), and a bone contact face.

The subroutine calculates the following parameters for every implant contact node: incremental shear micromotions ($Is\mu M$), incremental gap micromotions ($Ig\mu M$), resulting shear micromotions ($Rs\mu M$), and resulting gap micromotions ($Rg\mu M$). The process begins by restarting the four values of micromotions for each contact node if the cycle is about to begin (figure D.1 1). It is then followed by a for loop that obtains the closest bone element to that node, and stores that element's face as a reference system to calculate the shear and gap micromotions (figure D.1 2).

The, the current face normal vector $\overline{V}_n$ is stored, and its referred on the position of the contact node (figure D.1 3). Where the magnitude of this vector expresses the total gap between the node and the bone (incremental gap micromotions $Ig\mu M$). As the mesh of the bone uses tetrahedral elements, a local coordinate system is defined by the vectors ($\overline{V}_{ab}$ and $\overline{V}_{ac}$) that go from the first node of the element face (A) to the other two nodes (B and C), respectively. This system s used to locate the exact coordinates of the projection of the contact node into the bone face with the vector $\overline{V}_{ax}$ (figure D.1 4).

Both $\overline{V}_n$ and $\overline{V}_{ax}$ are then stored for each increment. After that, the current shear coordinates are compared to the coordinates of every previous increment, obtaining the total distances from the current increment to all the previous (figure D.1 5). Then, the incremental shear micromotions $Is\mu M$ were defined as the longest of these distances (figure D.1 6). Then, the current incremental shear micromotions $Is\mu M$ are compared to all the previous incremental values (figure D.1 7). If the current $Is\mu M$ was higher than all the previous values, then this was set as the resulting shear micromotions $Rs\mu M$ value (figure D.1 8). After that, the subroutine compares the current $Ig\mu M$ to all the previous incremental values. In the same fashion as with shear micromotions, if the $Ig\mu M$ is higher than all the previous increments, the current value would then become the new resulting gap micromotions $Rg\mu M$ (figure D.1 10).

After incremental micromotion analysis, the model calculated the loads and inner displacements via FEM (as a common simulation). The process would be repeated for every increment of the loading cycle. Finally, every simulation finished after four cycles were performed, as it has been proven that those are enough for resulting micromotions converge to its final value [93].

Bibliography

[1] R. Jared and M. Foran, *Total knee replacement.* American Academy of Orthopaedic surgeons (2015).

[2] J. Rand and D. Ilstrup, *Survivorship analysis of total knee arthroplasty. cumulative rates of survival of 9200 total knee arthroplasties.* The Journal of bone and joint surgery. American volume **73**, 397 (1991).

[3] R. E. Delanois, J. B. Mistry, C. U. Gwam, N. S. Mohamed, U. S. Choksi, and M. A. Mont, *Current epidemiology of revision total knee arthroplasty in the united states,* The Journal of arthroplasty **32**, 2663 (2017).

[4] M. A. Ritter, L. E. Eizember, R. W. Fechtman, E. M. Keating, and P. M. Faris, *Revision total knee arthroplasty: a survival analysis,* The Journal of arthroplasty **6**, 351 (1991).

[5] P. F. Sharkey, P. M. Lichstein, C. Shen, A. T. Tokarski, and J. Parvizi, *Why are total knee arthroplasties failing today—has anything changed after 10 years?* The Journal of arthroplasty **29**, 1774 (2014).

[6] P. F. Sharkey, W. J. Hozack, R. H. Rothman, S. Shastri, and S. M. Jacoby, *Why are total knee arthroplasties failing today?* Clinical Orthopaedics and Related Research® **404**, 7 (2002).

[7] W. Harris, A. Schiller, J. Scholler, R. Freiberg, and R. Scott, *Extensive localized bone resorption in the femur following total hip replacement,* JBJS **58**, 612 (1976).

[8] K. G. Vince, A. Abdeen, and T. Sugimori, *The unstable total knee arthroplasty: causes and cures,* The Journal of arthroplasty **21**, 44 (2006).

[9] P. W. Manner, *Knee replacement implants.* American Academy of Orthopaedic surgeons (2016).

[10] G. P. Duffy, D. J. Berry, and J. A. Rand, *Cement versus cementless fixation in total knee arthroplasty.* Clinical orthopaedics and related research **356**, 66 (1998).

[11] L. A. Whiteside, *Fixation for primary total knee arthroplasty,* The Journal of arthroplasty **11**, 125 (1996).

[12] M. A. Mont, R. Pivec, K. Issa, B. H. Kapadia, A. Maheshwari, and S. F. Harwin, *Long-term implant survivorship of cementless total knee arthroplasty: a systematic review of the literature and meta-analysis,* The journal of knee surgery **27**, 369 (2014).

[13] J. Charnley, *Acrylic cement in orthopaedic surgery,* in *Acrylic cement in orthopaedic surgery* (1970).

[14] P. A. Lotke and M. L. Ecker, *Influence of positioning of prosthesis in total knee replacement.* The Journal of bone and joint surgery. American volume **59**, 77 (1977).

[15] H.-G. Willert, J. Ludwig, and M. Semlitsch, *Reaction of bone to methacrylate after hip arthroplasty: a long-term gross, light microscopic, and scanning electron microscopic study,* JBJS **56**, 1368 (1974).

[16] S. B. Goodman, *The effects of micromotion and particulate materials on tissue differentiation: bone chamber studies in rabbits,* Acta Orthopaedica Scandinavica **65**, 1 (1994).

[17] C. A. Engh, D. O'connor, M. Jasty, T. F. McGovern, J. D. Bobyn, and W. H. Harris, *Quantification of implant micromotion, strain shielding, and bone resorption with porous-coated anatomic medullary locking femoral prostheses.* Clinical orthopaedics and related research , 13 (1992).

[18] M. Jasty, C. Bragdon, D. Burke, D. O'connor, J. Lowenstein, and W. H. Harris, *In vivo skeletal responses to porous-surfaced implants subjected to small induced motions,* JBJS **79**, 707 (1997).

[19] P. Aspenberg, S. Goodman, S. Toksvig-Larsen, L. Ryd, and T. Albrektsson, *Intermittent micromotion inhibits bone ingrowth: titanium implants in rabbits,* Acta Orthopaedica Scandinavica **63**, 141 (1992).

[20] P. J. Branson, J. W. Steege, R. L. Wixson, J. Lewis, and S. D. Stulberg, *Rigidity of initial fixation with uncemented tibial knee implants,* The Journal of arthroplasty **4**, 21 (1989).

[21] A.-B. Huang, H.-J. Wang, J.-K. Yu, B. Yang, D. Ma, and J.-Y. Zhang, *Are there any clinical and radiographic differences between quadriceps-sparing and mini-medial parapatellar approaches in total knee arthroplasty after a minimum 5 years of follow-up?* Chinese medical journal **128**, 1898 (2015).

[22] H. U. Cameron and G. A. Hunter, *Failure in total knee arthroplasty: mechanisms, revisions, and results.* Clinical orthopaedics and related research , 141 (1982).

[23] J. H. Bargren, J. Blaha, and M. Freeman, *Alignment in total knee arthroplasty. correlated biomechanical and clinical observations.* Clinical orthopaedics and related research , 178 (1983).

[24] J. A. Rand and M. Coventry, *Stress fractures after total knee arthroplasty.* JBJS **62**, 226 (1980).

[25] G. V. Green, K. R. Berend, M. E. Berend, R. R. Glisson, and T. P. Vail, *The effects of varus tibial alignment on proximal tibial surface strain in total knee arthroplasty: the posteromedial hot spot,* The Journal of arthroplasty **17**, 1033 (2002).

[26] M. E. Berend, M. A. Ritter, J. B. Meding, P. M. Faris, E. M. Keating, R. Redelman, G. W. Faris, and K. E. Davis, *The chetranjan ranawat award: Tibial component failure mechanisms in total knee arthroplasty.* Clinical orthopaedics and related research **428**, 26 (2004).

[27] D. Spicer, D. Pomeroy, W. Badenhausen, J. L. Schaper, J. Curry, K. Suthers, and M. Smith, *Body mass index as a predictor of outcome in total knee replacement,* International orthopaedics **25**, 246 (2001).

[28] M. A. Ritter, K. E. Davis, J. B. Meding, J. L. Pierson, M. E. Berend, and R. A. Malinzak, *The effect of alignment and bmi on failure of total knee replacement,* JBJS **93**, 1588 (2011).

[29] M. E. Berend, M. A. Ritter, H. C. Hyldahl, J. B. Meding, and R. Redelman, *Implant migration and failure in total knee arthroplasty is related to body mass index and tibial component size,* The Journal of arthroplasty **23**, 104 (2008).

[30] E. D. Z. van Rilland, J. C. Varcadipane, O. Geling, M. M. Kuba, and C. K. Nakasone, *A minimum 2-year follow-up using modular trabecular metal tibial components in total knee arthroplasty,* Reconstructive Review **5** (2015).

[31] J. Wolff, *The law of bone remodelling. 1986,* Originally published in (1870).

[32] I. Oh and W. H. Harris, *Proximal strain distribution in the loaded femur. an in vitro comparison of the distributions in the intact femur and after insertion of different hip-replacement femoral components.* The Journal of bone and joint surgery. American volume **60**, 75 (1978).

[33] S. Cowin and D. Hegedus, *Bone remodeling i: theory of adaptive elasticity,* Journal of Elasticity **6**, 313 (1976).

[34] D. Hegedus and S. Cowin, *Bone remodeling ii: small strain adaptive elasticity,* Journal of elasticity **6**, 337 (1976).

[35] G. Beaupré, T. Orr, and D. Carter, *An approach for time-dependent bone modeling and remodeling—theoretical development,* Journal of Orthopaedic Research **8**, 651 (1990).

[36] C. R. Jacobs, J. C. Simo, G. S. Beaupre, and D. R. Carter, *Adaptive bone remodeling incorporating simultaneous density and anisotropy considerations,* Journal of biomechanics **30**, 603 (1997).

[37] M. Doblaré and J. Garcıa, *Anisotropic bone remodelling model based on a continuum damage-repair theory,* Journal of biomechanics **35**, 1 (2002).

[38] R. Huiskes, H. Weinans, H. Grootenboer, M. Dalstra, B. Fudala, and T. Slooff, *Adaptive bone-remodeling theory applied to prosthetic-design analysis,* Journal of biomechanics **20**, 1135 (1987).

[39] D. Kluess, *Finite element analysis in orthopaedic biomechanics,* in *Finite Element Analysis* (InTech, 2010).

[40] R. Huiskes and E. Chao, *A survey of finite element analysis in orthopedic biomechanics: the first decade,* Journal of biomechanics **16**, 385 (1983).

[41] B. van der Ploeg, M. Tarala, J. Homminga, D. Janssen, P. Buma, and N. Verdonschot, *Toward a more realistic prediction of peri-prosthetic micromotions,* Journal of orthopaedic research **30**, 1147 (2012).

[42] D. Y. Chong, U. N. Hansen, and A. A. Amis, *Analysis of bone–prosthesis interface micromotion for cementless tibial prosthesis fixation and the influence of loading conditions,* Journal of biomechanics **43**, 1074 (2010).

[43] S. Berahmani, D. Janssen, D. Wolfson, M. de Waal Malefijt, C. K. Fitzpatrick, P. J. Rullkoetter, and N. Verdonschot, *Fe analysis of the effects of simplifications in experimental testing on micromotions of uncemented femoral knee implants,* Journal of orthopaedic research **34**, 812 (2016).

[44] G. Bergmann and F. Graichen, *Orthoload, loading of orthopaedic implants,* Orthoload (2008).

[45] R. Rakotomanana, P. Leyvraz, A. Curnier, J. Heegaard, and P. Rubin, *A finite element model for evaluation of tibial prosthesis-bone interface in total knee replacement,* Journal of Biomechanics **25**, 1413 (1992).

[46] J. H. Keyak, S. A. Rossi, K. A. Jones, and H. B. Skinner, *Prediction of femoral fracture load using automated finite element modeling,* Journal of biomechanics **31**, 125 (1997).

[47] E. F. Morgan, H. H. Bayraktar, and T. M. Keaveny, *Trabecular bone modulus–density relationships depend on anatomic site,* Journal of biomechanics **36**, 897 (2003).

[48] E. F. Morgan and T. M. Keaveny, *Dependence of yield strain of human trabecular bone on anatomic site,* Journal of biomechanics **34**, 569 (2001).

[49] J. Keyak, I. Lee, and H. Skinner, *Correlations between orthogonal mechanical properties and density of trabecular bone: use of different densitometric measures,* Journal of Biomedical Materials Research Part A **28**, 1329 (1994).

[50] J. H. Keyak and Y. Falkinstein, *Comparison of in situ and in vitro ct scan-based finite element model predictions of proximal femoral fracture load,* Medical Engineering and Physics **25**, 781 (2003).

[51] J. H. Keyak, T. S. Kaneko, J. Tehranzadeh, and H. B. Skinner, *Predicting proximal femoral strength using structural engineering models.* Clinical orthopaedics and related research **437**, 219 (2005).

[52] S. Berahmani, D. Janssen, and N. Verdonschot, *Experimental and computational analysis of micromotions of an uncemented femoral knee implant using elastic and plastic bone material models,* Journal of biomechanics **61**, 137 (2017).

[53] N. Kelly and J. P. McGarry, *Experimental and numerical characterisation of the elasto-plastic properties of bovine trabecular bone and a trabecular bone analogue,* Journal of the mechanical behavior of biomedical materials **9**, 184 (2012).

[54] N. Kelly, N. M. Harrison, P. McDonnell, and J. P. McGarry, *An experimental and computational investigation of the post-yield behaviour of trabecular bone during vertebral device subsidence,* Biomechanics and modeling in mechanobiology **12**, 685 (2013).

[55] G. Poumarat and P. Squire, *Comparison of mechanical properties of human, bovine bone and a new processed bone xenograft,* Biomaterials **14**, 337 (1993).

[56] M. Tissakht, H. Eskandari, and A. Ahmed, *Micromotion analysis of the fixation of total knee tibial component,* Computers & structures **56**, 365 (1995).

[57] A. Hashemi and A. Shirazi-Adl, *Finite element analysis of tibial implants—effect of fixation design and friction model,* Computer methods in biomechanics and biomedical engineering **3**, 183 (2000).

[58] C. K. Fitzpatrick, P. Hemelaar, and M. Taylor, *Computationally efficient prediction of bone–implant interface micromotion of a cementless tibial tray during gait,* Journal of biomechanics **47**, 1718 (2014).

[59] J. Hanzlik, J. Day, S. Kurtz, N. Verdonschot, and D. Janssen, *Does implant design, bone quality and activity type affect micromotion at the bone-porous tantalum tibial tray interface?* Bone Joint J **98**, 26 (2016).

[60] S. E. Clift, *Finite element modeling of uncemented implants: Challenges in the representation of the press-fit condition,* in *13th International Conference on Biomedical Engineering* (Springer, 2009) pp. 1608–1610.

[61] G. Selvik, *Roentgen stereophotogrammetry: a method for the study of the kinematics of the skeletal system,* Acta Orthopaedica Scandinavica **60**, 1 (1989).

[62] M. G. Li and K. G. Nilsson, *The effect of the preoperative bone quality on the fixation of the tibial component in total knee arthroplasty,* The Journal of arthroplasty **15**, 744 (2000).

[63] M. Stilling, F. Madsen, A. Odgaard, L. Rømer, N. T. Andersen, O. Rahbek, and K. Søballe, *Superior fixation of pegged trabecular metal over screw-fixed pegged porous titanium fiber mesh: a randomized clinical rsa study on cementless tibial components,* Acta orthopaedica **82**, 177 (2011).

[64] D. A. Wilson, G. Richardson, A. W. Hennigar, and M. J. Dunbar, *Continued stabilization of trabecular metal tibial monoblock total knee arthroplasty components at 5 years—measured with radiostereometric analysis,* Acta orthopaedica **83**, 36 (2012).

[65] A. Henricson, L. Linder, and K. G. Nilsson, *A trabecular metal tibial component in total knee replacement in patients younger than 60 years: a two-year radiostereophotogrammetric analysis,* Bone & Joint Journal **90**, 1585 (2008).

[66] A. Henricson, D. Rösmark, and K. G. Nilsson, *Trabecular metal tibia still stable at 5 years: an rsa study of 36 patients aged less than 60 years,* Acta orthopaedica **84**, 398 (2013).

[67] G. Bergmann, F. Graichen, and A. Rohlmann, *Hip joint contact forces during stumbling,* Langenbeck's Archives of Surgery **389**, 53 (2004).

[68] A. Perillo-Marcone, D. Barrett, and M. Taylor, *The importance of tibial alignment: finite element analysis of tibial malalignment,* The Journal of arthroplasty **15**, 1020 (2000).

[69] J.-J. Liau, C.-K. Cheng, C.-H. Huang, and W.-H. Lo, *The effect of malalignment on stresses in polyethylene component of total knee prostheses–a finite element analysis,* Clinical Biomechanics **17**, 140 (2002).

[70] B. Innocenti, J. Bellemans, and F. Catani, *Deviations from optimal alignment in tka: is there a biomechanical difference between femoral or tibial component alignment?* The Journal of arthroplasty **31**, 295 (2016).

[71] D. Dabirrahmani, J. Rooney, R. Appleyard, and M. Gillies, *Adaptive bone remodelling following total knee arthroplasty: a finite element study,* J Bone Joint Surg (2010).

[72] D. T. Cawley, N. Kelly, A. Simpkin, F. J. Shannon, and J. P. McGarry, *Full and surface tibial cementation in total knee arthroplasty: a biomechanical investigation of stress distribution and remodeling in the tibia,* Clinical biomechanics **27**, 390 (2012).

[73] D. Y. Chong, U. N. Hansen, R. Van der Venne, N. Verdonschot, and A. A. Amis, *The influence of tibial component fixation techniques on resorption of supporting bone stock after total knee replacement,* Journal of Biomechanics **44**, 948 (2011).

[74] Y. Minoda, A. Kobayashi, M. Ikebuchi, H. Iwaki, F. Inori, and H. Nakamura, *Porous tantalum tibial component prevents periprosthetic loss of bone mineral density after total knee arthroplasty for five years—a matched cohort study,* The Journal of arthroplasty **28**, 1760 (2013).

[75] J. A. Hanzlik, J. S. Day, C. M. Rimnac, and S. M. Kurtz, *Is there a difference in bone ingrowth in modular versus monoblock porous tantalum tibial trays?* The Journal of arthroplasty **30**, 1073 (2015).

[76] D. D. Cook and D. J. Robertson, *The generic modeling fallacy: average biomechanical models often produce non-average results!* Journal of biomechanics **49**, 3609 (2016).

[77] W. W. Hauck and S. Anderson, *A new statistical procedure for testing equivalence in two-group comparative bioavailability trials,* Journal of Pharmacokinetics and Biopharmaceutics **12**, 83 (1984).

[78] *510k summary of safety and effectiveness. zimmer persona personalized knee system.* Food and Drugs Administration. (2012).

[79] *Class 2 device recall persona trabecular metal tibial plate persona tm tibia,* Food and Drugs Administration. (2015).

[80] W. F. Zimmerman, M. A. Miller, R. J. Cleary, T. H. Izant, and K. A. Mann, *Damage in total knee replacements from mechanical overload,* Journal of biomechanics **49**, 2068 (2016).

[81] *Zimmer nexgen trabecular metal monoblock tibial components surgical technique addendum,* Zimmer. (2007).

[82] *Zimmer nexgen cr and lps trabecular metal monoblock tibias, addendum,* Zimmer. (2003).

[83] *Persona the personalized knee system trabecular metal tibial component surgical technique,* Zimmer. (2014).

[84] *Persona the personalized knee system tibial component product profiler,* Zimmer. (2012).

[85] R. Hill, *A general theory of uniqueness and stability in elastic-plastic solids,* Journal of the Mechanics and Physics of Solids **6**, 236 (1958).

[86] M. Ding, M. Dalstra, C. C. Danielsen, J. Kabel, I. Hvid, and F. Linde, *Age variations in the properties of human tibial trabecular bone,* J Bone Joint Surg Br **79**, 995 (1997).

[87] V. Deshpande and N. Fleck, *Isotropic constitutive models for metallic foams,* Journal of the Mechanics and Physics of Solids **48**, 1253 (2000).

[88] H. Weinans, R. Huiskes, B. Van Rietbergen, D. Sumner, T. Turner, and J. Galante, *Adaptive bone remodeling around bonded noncemented total hip arthroplasty: a comparison between animal experiments and computer simulation,* Journal of Orthopaedic Research **11**, 500 (1993).

[89] *Zimmer nexgen trabecular metal modular tibial component addendum,* Zimmer. (2007).

[90] D. Lacroix and P. Prendergast, *A mechano-regulation model for tissue differentiation during fracture healing: analysis of gap size and loading,* Journal of biomechanics **35**, 1163 (2002).

[91] W. T. Koiter, *General theorems for elastic-plastic solids* (North-Holland Amsterdam, 1960) pp. 165–221.

[92] *Marc 2015 volume d: User subroutines and special subroutines,* MSC Software (2015).

[93] S. Berahmani, *Press-fit stability of cementless femoral knee implants. A biomechanical evaluation*, Ph.D. thesis, [Sl: sn] (2017).